

Enhanced Removal of Mercury and Lead by a Novel and Efficient Surface-functionalized Imogolite with Nanoscale Zero-valent Iron Material

Estefanía Martinis (✉ emartinis@mendoza-conicet.gob.ar)

CONICET: Consejo Nacional de Investigaciones Cientificas y Tecnicas

Juliano Denardin

CEDENNA

Raul Calderón Raul Calderón

Universidad Bernardo O'Higgins

Cristóbal Flores

Universidad de Santiago de Chile

Karen Manquián-Cerda

Universidad de Santiago de Chile

Tamara Maldonado

Universidad de Santiago de Chile

Nicolás Arancibia-Miranda

Universidad de Santiago de Chile

Research Article

Keywords: Imogolite, Nanoscale zero valent iron (nZVI), Hybrid material, Neurotoxic metals (Hg and Pb) removal

Posted Date: May 28th, 2021

DOI: <https://doi.org/10.21203/rs.3.rs-526809/v1>

License: © ⓘ This work is licensed under a Creative Commons Attribution 4.0 International License.

[Read Full License](#)

Version of Record: A version of this preprint was published at Environmental Science and Pollution Research on November 2nd, 2021. See the published version at <https://doi.org/10.1007/s11356-021-17242-7>.

19 **ABSTRACT**

20 A novel hybrid nanomaterial, nanoscale zero-valent iron (nZVI)-grafted imogolite
21 nanotubes (Imo), was synthesized via a fast and straightforward chemical procedure. The
22 as-obtained nanomaterial (Imo-nZVI) was characterized using transmission electron
23 microscopy (TEM), electrophoretic mobility (EM) and vibrating sample magnetometry
24 (VSM). The prepared Imo-nZVI was superparamagnetic at room temperature and could
25 be easily separated by an external magnetic field. Sorption batch experiments were
26 performed in single- and multicomponent system and showed that Hg^{2+} and Pb^{2+} could
27 be quantitatively adsorbed at pH 4.0 with maximum adsorption capacities of 62.3 and
28 73.8 $\text{mg} \cdot \text{g}^{-1}$, respectively. It was observed that the functional groups in Imo-nZVI interact
29 preferentially with analytes according to Misono Softness parameter. The higher
30 performance of Imo-nZVI compared with Imo and nZVI is related to the increased
31 adsorption sites in the functionalized nanomaterial. The sorption equilibrium data obeyed
32 the Langmuir model, while kinetic studies demonstrated that the sorption processes of
33 Hg^{2+} and Pb^{2+} followed the pseudo-second-order model. This study suggests that the Imo-
34 nZVI composite can be used as a promising sorbent and provides a simple and fast
35 separation method for the removal of Hg and Pb ions from contaminated water.

36 **Keywords:** *Imogolite; Nanoscale zero valent iron (nZVI); Hybrid material; Neurotoxic*
37 *metals (Hg and Pb) removal*

38 1. Introduction

39 Nanoscale zero-valent iron (nZVI) has recently emerged as powerful and versatile
40 sorbents for potential use in environmental engineering. Because of their special
41 physicochemical properties, such as a high surface-to-volume ratio, magnetism and in
42 situ reactivity, nZVI materials have attracted substantial interest in the scientific
43 community. nZVI has shown application in a wide array of environmental treatments,
44 such as soil, sediment, and groundwater remediation (Crane & Scott 2012, Li et al. 2006,
45 Stefaniuk et al. 2016, Yan et al. 2010). However, nZVI forms aggregates due to van der
46 Waals and magnetic forces, which decrease its efficiency by reducing its surface area and
47 producing a less negative oxidation–reduction potential (Shi et al. 2011). Different
48 approaches based on immobilization techniques have been developed for nZVI
49 stabilization. Diatomite, zeolites, montmorillonite or cellulose have been used as matrices
50 to increase the stability of nZVI (Arancibia-Miranda et al. 2016, Bossa et al. 2017, Dror
51 et al. 2012, Kim et al. 2013, Suazo-Hernández et al. 2020, Suazo-Hernández et al. 2019,
52 Zou et al. 2016). Furthermore, the sorption capacity of nZVI can also be improved by
53 synergistically combining it with other nanomaterials. In this sense, inorganic nanotubes
54 based on aluminosilicates, called imogolite (Imo), have attracted much research attention
55 due to their one-dimensional structure, mechanical resistance and reactive surfaces
56 (Arancibia-Miranda et al. 2020, Arancibia-Miranda et al. 2015). Imogolite is a hydrated
57 aluminosilicate with the chemical formula $(\text{OH})_3\text{Al}_2\text{O}_3\text{SiOH}$ (Cradwick et al. 1972).
58 Characterized as a nanotubular structure, imogolite has a variable length from 100 nm to
59 several microns, an internal diameter of 1 nm, and an external diameter of 2 nm for natural
60 Imo, whereas synthetic Imo has a diameter in the range of 2.3–2.7 nm according to the
61 synthesis method (Arancibia-Miranda et al. 2013b). Imogolite is amphoteric because the
62 inner surface of nanotubes is lined with isolated silanol ($\equiv\text{SiOH}$) groups, and the outer

63 surface of nanotubes is covered with both Al–O–Al and Al–OH–Al groups, determining
64 the superficial properties of this material (Arancibia-Miranda et al. 2017). Because of its
65 high dispersibility in water and the amphoteric character of Imo, which is strongly
66 influenced by the pH of the medium (Arancibia-Miranda et al. 2015), cations should be
67 able to interact with the inner surface and anions with the outer surface of the nanotubes
68 (Bonelli 2016). Due to the special properties of imogolite, this nanomaterial has attracted
69 substantial interest in the scientific community because of its potential application in the
70 removal of cations and anions from polluted water (Arancibia-Miranda et al. 2020,
71 Bonelli 2016, Levard et al. 2009).

72 In this work, we propose the functionalization of imogolite with nZVI as a strategy to
73 obtain a powerful and new sorbent nanomaterial with magnetic properties. The
74 combination of both nanomaterials can be synergistically used to enhance the extraction
75 efficiency of certain analytes (Bonelli 2016). In this context, recent research has shown
76 that the high reactivity of nZVI promotes the stabilization of potential contaminants
77 through multiple processes, such as adsorption, reduction, oxidation, precipitation and
78 coprecipitation (Jiang et al. 2018, Lu et al. 2016). However, it is important to consider
79 that mechanisms of removal for nZVI are dependent on conditions of the media (pH and
80 redox potential (E_h)), but also on the type, chemical status, and nature of the analyte. In
81 this sense, the sorption preferences and specific interactions between the substrate and
82 the analyte are dependent on (i) the hydrolysis constant of the metal ion (considering the
83 presence of $\equiv X-OH$ and $\equiv X-O-OH$ groups), (ii) polarizability, (iii) ionic and hydrated
84 radius, and (iv) trend to form covalent bonds. In this context, Sposito (1989) postulated a
85 relationship for an atom, defined as the Misono softness parameter, to form covalent
86 bonds according to its ionic radius and ionization potential (Sposito 1989). A large
87 Misono softness value for an atom indicates its preference for electrostatic and inner-

88 sphere surface complexation reactions. In this work, the removal of Hg and Pb from water
89 samples was studied. Hg and Pb have long been a worrying issue due to their high
90 neurotoxicity and widespread occurrence (Charlet et al. 2012, Jaishankar et al. 2014). The
91 potential health risks from low levels of Hg and Pb are a subject of intense debate.
92 Therefore, removal of these two metals from water samples is a current challenge. Taking
93 these factors into consideration, along with the potential advantages resulting from the
94 combination of imogolite and nZVI, synthesis and characterization of the hybrid
95 nanomaterial and kinetic extraction studies of Hg^{2+} and Pb^{2+} are presented.

96 **2. Experimental**

97 **2.1. Instrumentation**

98 Elemental detection was performed using a PerkinElmer 5100ZL atomic absorption
99 spectrometer (PerkinElmer, Norwalk, CT, USA) equipped with a pyrolytic graphite tube
100 and a transversely heated graphite atomizer Zeeman-effect background correction system
101 (PerkinElmer, Norwalk, CT, USA). Hg and Pb electrodeless discharge lamps (EDL)
102 (PerkinElmer) operated at currents of 170 mA and 360 mA (modulated operation) and
103 wavelengths of 253.7 nm and 283.3 nm, respectively, with a spectral bandpass of 0.7 nm,
104 were used. All measurements were made based on absorbance signals with an integration
105 time of 5 s.

106 A centrifuge (model 5810, Eppendorf, Germany) was used to accelerate the phase
107 separation process. A reciprocating shaker (Boeco, Hamburg, Germany) was used to mix
108 the reagents. A Horiba F-51 pH meter (Kyoto, Japan) was used for pH determinations.

109 **2.2. Reagents**

110 All reagents were of analytical grade, and the presence of Hg was not detected within the
111 working range. A 1000 $\mu\text{g mL}^{-1}$ Hg^{2+} stock solution was prepared from mercury(II)
112 nitrate (Merck, Darmstadt, Germany) in 0.1 mol L^{-1} HNO_3 (Ultrex[®] II Mallinckrodt
113 Baker, Phillipsburg, NJ, USA). Lower concentrations of Hg^{2+} were prepared by diluting
114 the stock solution with 0.1 mol L^{-1} HNO_3 . A 1000 $\mu\text{g mL}^{-1}$ Pb^{2+} stock solution was
115 prepared from lead(II) nitrate (Merck, Darmstadt, Germany) in 0.1 mol L^{-1} HNO_3 . Stock
116 solutions of 150 mg L^{-1} $\text{Mg}(\text{NO}_3)_2$ (Merck) and 2500 mg L^{-1} $\text{NH}_4\text{H}_2\text{PO}_4$ (Merck) were
117 prepared and used as chemical modifiers. These solutions were prepared in 0.1% (v/v)
118 HNO_3 . A KNO_3 (Merck) solution (2 mol L^{-1}) was used to adjust the ionic strength.
119 Ultrapure water (18 $\text{M}\Omega$ cm) was obtained from a Millipore Continental Water System
120 (Bedford, MA, USA).

121 For the synthesis of Imo, the reagents used were tetraethyl orthosilicate (99.995%,
122 Sigma–Aldrich), NaOH (99.996%, Merck), and $\text{Al}(\text{NO}_3)_3 \cdot 9\text{H}_2\text{O}$ (99.998%, Merck). The
123 coating procedure involved the use of $\text{Fe}(\text{NO}_3)_3 \cdot 6\text{H}_2\text{O}$ (99.998%, Merck), NaBH_4
124 (99.997%, Sigma–Aldrich) and absolute ethanol (Merck). In sorption studies, KNO_3
125 (99.998%, Merck) was used. When needed, reagent grade solvents were considered.
126 Ultrapure water (18 $\text{M}\Omega$ cm) was obtained from a Millipore Continental Water System
127 (Bedford, MA, USA). All reactions were conducted at ambient conditions.

128 **2.3. Synthesis of imogolite**

129 Imo was prepared according to the procedure described by Arancibia-Miranda et al.
130 (Arancibia-Miranda et al. 2011).

131 **2.4. Synthesis of nZVI and nZVI functionalized imogolite**

132 nZVI was synthesized according to Arancibia-Miranda et al. procedure.[7] The new Imo-
133 nZVI was obtained as follow: the coating process had a theoretical 2:1 mixture of Imo/Fe
134 (w/w), obtained by dissolving 24.41 g of $\text{Fe}(\text{NO}_3)_3 \cdot 6\text{H}_2\text{O}$ in 100 mL of EtOH:H₂O
135 (90:10) in a 500 mL round bottom flask. Then, Imo (2.50 g) suspended in 100 mL of
136 EtOH:H₂O (9:1) was added. The suspension was stirred for 3 h, leading to a lighter
137 orange-red solution. The NaBH₄ reducing agent (20.0 g) dissolved in 100 mL of H₂O was
138 immediately added at room temperature, causing the solution to turn black within 30-60
139 s, and the reaction mixture was stirred for approximately 1 h under a N₂ atmosphere. The
140 product was collected in a Falcon tube and centrifuged. The supernatant was removed,
141 and the precipitated product was cleaned with an ethanol EtOH:H₂O (9:1) solution several
142 times. Finally, the product was frozen with liquid N₂ and lyophilized.

143 **Characterization**

144 The products were characterized by X-ray diffraction (XRD), transmission electron
145 microscopy (TEM), electrophoretic mobility (EM) and vibrating sample magnetometry
146 (VSM). The samples were studied on a diffractometer (Shimadzu XRD-6000) at 1.5418
147 Å with CuK α radiation in the 2 θ region of 5–80°. A Zeiss EM 910 transmission electron
148 microscope using an 80 kV acceleration potential on carbon substrates was prepared as
149 follows: A drop of the sample suspended in water was transferred onto the face of a
150 freshly cleaved sheet of mica, and the solvent was allowed to evaporate.

151 The magnetic response of the samples was investigated with a vibrating sample
152 magnetometer (VSM) operated at room temperature with a maximum magnetic field of
153 1.2 Tesla and a sensitivity of 10⁻⁴ emu. The isoelectric point (IEP) was determined by
154 measuring the zeta potential of particles on a Zeta Meter ZM-4.0 apparatus.
155 Approximately 30 mg of each sample was suspended in 200 mL of a solution with an

156 ionic strength of $0.01 \text{ mol}\cdot\text{L}^{-1}$ (KNO_3), and the EM was determined as a function of pH.
157 The IEP was obtained from the EM versus pH graph as the pH at which $\text{EM} = 0$. The
158 specific surface areas (SSAs) of imogolite, nZVI and Imo-nZVI were measured by the
159 N_2 method of Brunauer-Emmett-Teller (BET), and pore size was calculated from Barrett,
160 Joyner and Halenda (BJH) analysis of N_2 adsorption/desorption isotherms at 77 K using
161 an automatic analyzer (Quantachrome Nova Station A, Quantachrome, USA, Florida).

162 **2.5. Sorption studies**

163 Batch adsorption of Pb^{2+} and Hg^{2+} was studied in 40 mL polypropylene centrifuge tubes
164 containing 10 mg of imogolite and Imo-nZVI in 10 mL of a Hg^{2+} or Pb^{2+} solution in 0.01
165 $\text{mol}\cdot\text{L}^{-1}$ KNO_3 , respectively. The dependence of metal adsorption as a function of time
166 was studied in a solution of Pb or Hg containing $60 \text{ mg}\cdot\text{L}^{-1}$ in equilibrium with 10 mg of
167 imogolite and Imo-nZVI. The samples were equilibrated using a reciprocating shaker for
168 300 min. The temperature for the experiments was 298 K, and the pH condition was 3.0
169 ± 0.2 for both metals (see Table S1). The samples were centrifuged at 10,000 rpm for 10
170 min, and the supernatant was filtered through 0.22 mm Millex-GX membranes and
171 analyzed by ETAAS. The amount of adsorbed metals was determined from the difference
172 between the initial and final concentrations in solution, according to Eq. (1).

$$173 \quad q_t = \frac{(C_o - C_t)V}{M} \quad (1)$$

174 where C_o and C_t are the initial metal concentrations in $\text{mg}\cdot\text{L}^{-1}$ and at time t , respectively;
175 V (L) is the volume; and M (g) is the mass of the substrate.

176 **2.6. Sorption kinetics models**

177 *Pseudo-first-order model (PFO)*

178 In this model, the kinetic rate equation is given by:

179 $\frac{dq_t}{dt} = k_1(q_e - q_t)$ (2)

180 where q_e and q_t correspond to the amount adsorbed and in equilibrium at time t , expressed
181 in $\text{mg}\cdot\text{g}^{-1}$, respectively, and k_1 is the pseudo-first-order adsorption rate constant (min^{-1}),
182 which is a combination of the adsorption (k_a) and desorption (k_d) constants (Boparai et
183 al. 2011, Lagergren 2013, Manquían-Cerda et al. 2017, Rudzinski &Panczyk 2000).

184 Integration of this equation from $t = 0$ to $t = t$ and $q = 0$ to $q = q$ gives

185 $\log(q_e - q_t) = \log(q_e) - \frac{k_1}{2.303}t$ (3)

186 *Pseudo-second-order model (PSO)*

187 In this case, the driving force ($q_e - q_t$) is proportional to the portion of activated sites
188 available on the sorbent (Ho &McKay 2000, Rao et al. 2006, Rudzinski &Plazinski 2008).

189 The kinetic rate equation follows the expression:

190 $\frac{dq_t}{dt} = k_2(q_e - q_t)^2$ (4)

191 Rearranging the variables in this equation and integrating between times 0 and t and the
192 corresponding boundary conditions 0 and q gives:

193 $\frac{t}{q_t} = \frac{1}{q_e^2 k_2} + \frac{1}{q_e}t$ (5)

194 The initial adsorption rate of the system can be estimated by this model and determined
195 by $h = k \cdot q_e^2$, obtained directly from the intercept of the curve.

196 *Elovich equation*

197 This model is used to describe the chemisorption processes on heterogeneous surfaces; it
198 considers that adsorption takes place in two stages: a fast reaction, mainly associated with
199 the movement of the adsorbate over outer active sites, and diffusion (slow) into and out
200 of the adsorbent pores (Arancibia-Miranda et al. 2020, Arancibia-Miranda et al. 2015,
201 Chien &Clayton 1980, Wu et al. 2001, 2009). This model is expressed as:

202 $\frac{dq_t}{dt} = \alpha \exp(-\beta q_t)$ (6)

203 The constant α ($\text{mg} \cdot \text{g}^{-1} \cdot \text{min}^{-1}$) is regarded as the initial rate, and parameter β ($\text{g} \cdot \text{mg}^{-1}$) is
204 an indication of the number of sites available for adsorption, which is related to the extent
205 of surface coverage and activation energy for chemisorption. Given that $q_t = 0$ at $t = 0$,
206 the integrated form is:

207 $q_t = \left(\frac{1}{\beta}\right) \ln(\alpha\beta) + \frac{1}{\beta} \ln t$ (7)

208 Parameters α and β are obtained from the slope and intercept of the q_t vs. $\ln t$ plot,
209 respectively.

210 *Intraparticle diffusion model (Weber-Morris model)*

211 Weber-Morris's pore-diffusion model is a single-resistance model derived from Fick's
212 second law of diffusion (Cáceres-Jensen et al. 2013, Cheung et al. 2007, Weber & Morris
213 1963). If the sorption process is considered to be influenced by diffusion in the sorbent
214 and by convective diffusion in the sorbate solution, then the mathematical dependence of
215 sorbate uptake, q_t , at $t^{1/2}$ is given by the equation:

216 $q_t = k_{\text{int}} t^{1/2} + C$ (8)

217 where k_{int} ($\text{mg} \cdot \text{g}^{-1} \cdot \text{min}^{-1/2}$) is the intraparticle diffusion constant and C is a constant related
218 to the thickness of the surface layer; the higher the value of C obtained from the q_t vs. $t^{1/2}$
219 plot, the greater the boundary layer effect, which is related to intraparticle diffusivity.

220 *Langmuir Isotherm*

221 This model assumes that the analyte is adsorbed in a determined number of active sites,
222 forming a monolayer. The Langmuir equation is described by

223 $q_e = \frac{q_m K_L C_e}{1 + K_L C_e}$ (9)

224 where q_m ($\text{mg}\cdot\text{g}^{-1}$) is the maximum adsorption capacity, q_e (mg g^{-1}) is the amount of
225 analyte adsorbed, K_L is the Langmuir constant and C_e is the equilibrium molar
226 concentration of the analyte ($\text{mg}\cdot\text{L}^{-1}$).

227 **3. Results and discussion**

228 **3.1.Characterization of the composite**

229 The samples were analyzed by X-ray diffraction to evaluate the changes generated from
230 the coating process of imogolite with nZVI and Hg and Pb removal in single and
231 multicomponent systems (Fig. S1). For imogolite, four broad peaks were identified at
232 21.0, 12.0, 3.4, and 2.2 Å, corresponding to the (hkl) (100), (110), (001), and (211) planes,
233 respectively. According to previous reports, these planes are associated with monoclinic
234 or hexagonal packaging (Arancibia-Miranda et al. 2013a, Kang et al. 2014). In the case
235 of nZVI, diffraction peaks at $2\theta = 45.0^\circ$ (corresponding to the 110 plane) and $2\theta = 65.5^\circ$
236 (corresponding to the 200 plane) were observed, which also correspond to elemental Fe
237 (Arancibia-Miranda et al. 2016, Kanel et al. 2005, Zhang et al. 2011). Fe oxide diffraction
238 peaks were determined in nZVI, corresponding to magnetite and maghemite. The
239 diffractogram of composite Imo-nZVI showed bands attributed to imogolite and nZVI,
240 with clear differences in the degree of crystallinity of the peak in comparison to the
241 starting materials. No signs of Fe oxides were observed in the composite, suggesting that
242 nZVI oxidation did not occur or that the percentage of Fe oxide was less than the detection
243 capacity of the XRD equipment. The process of Hg and Pb removal in single and
244 multicomponent systems caused significant changes in the degree of crystallinity of the
245 composites, altering the structure of the immobilized nZVIs in imogolite. After the
246 removal process (single and multicomponent), the corrosion products magnetite (Fe_3O_4)
247 and lepidocrocite ($\gamma\text{-FeOOH}$) (Baltazar et al. 2014, Kanel et al. 2005) were identified

248 (Fig. S1). Both species are byproducts of the energetically favorable redox reactions
249 between the nZVI and the analytes, as is described in equations 10 and 11.



252

253 However, according to the significant differences in the standard redox potential for
254 Pb^{2+}/Pb^0 (-0.12 V) and $Hg(II)/Hg(0)$ (0.86 V) couples with respect to the $Fe^0/Fe^{(II)}$ (-0.44
255 V) couple, the removal of Hg^{2+} occurs preferentially by a reductive precipitation at the
256 nZVI surface (Lagergren 2013), whereas that removal process of Pb^{2+} occurs by sorption
257 with partial chemical reduction (Noubactep 2008).

258 It is important to highlight that in the multicomponent system, the samples have a lower
259 degree of crystallinity, which shows that the presence of both metals significantly alters
260 the surface of nZVI.

261 The morphologies of the samples were obtained through a detailed microscopic analysis
262 (Fig. 1). The dimensions of imogolite were determined by images retrieved by HR-TEM.
263 The external diameter was approximately 2 nm, with a length that exceeded 500 nm. For
264 nZVI, two clearly defined areas were observed. The first area presented a higher degree
265 of crystallinity located in the nucleus, corresponding to metallic Fe, while on the external
266 surface, there was a second amorphous area associated with iron oxides, a process widely
267 described in the literature. The coating process of imogolite with nZVI showed a
268 heterogeneous distribution, in which areas with a high presence of agglomerated nZVI
269 are highlighted. This is due to the synthesis conditions of nZVI, where the acid character
270 of Fe (Lewis acid) favors positive charges at superficial sites of imogolite, decreasing the
271 adsorption of this cation, which occurs at sites of greater specificity, a phenomenon

272 similar to that reported by Arancibia-Miranda et al., 2014. The dimensions of nZVI were
273 also sensitive to the process of its immobilization in imogolite, and the size was 20%
274 lower than that of nZVI synthesized without support.

275 The surface behavior of the study materials was described through measurements of zeta
276 potential (ZP) (Fig. 2), a technique that is sensitive to the changes that a surface can suffer
277 in its composition. The isoelectric point is considered an indicative parameter of what
278 occurs on the surface of imogolite due to being coated with nZVI. Imogolite has a pH-
279 sensitive surface charge and is positive over a wide pH range with an IEP value of 10.5,
280 which favors anion adsorption (Arancibia-Miranda et al. 2011). On the other hand, this
281 parameter of nZVI reached a value of 7.7, which is characteristic of this type of material.
282 The coating process with nZVI caused a drastic change in the IEP value of Imo-nZVI,
283 which presented a value of 8.3, in addition to a decrease in the magnitude of the generated
284 surface charge. The decrease in the IEP value observed in the composite reduces the
285 potential electrostatic impediments in the processes of divalent ion sorption, as occurs in
286 imogolite. The textural properties of the samples (Table 1) show that as a result of coating,
287 the SSA and pore volume decrease while the pore diameter increases.

288 The hysteresis curve of presorption Imo-nZVI shows a typical ferromagnetic curve with
289 a saturation magnetization (M_s) of $16.5 \text{ emu} \cdot \text{g}^{-1}$ and a coercive field (H_c) of 100 Oe (Fig.
290 S2). The Pb postsorption magnetization curve presents a decrease in M_s to $7 \text{ emu} \cdot \text{g}^{-1}$.
291 This decrease in magnetization is attributed to the amount of Pb that has been absorbed
292 by the Imo-nZVI nanoparticles, which does not contribute to the magnetization of the
293 sample. A much larger decrease in M_s is observed for the postsorption samples with Hg
294 and Pb-Hg, with values of $0.6 \text{ emu} \cdot \text{g}^{-1}$ and $0.56 \text{ emu} \cdot \text{g}^{-1}$, respectively. The coercivity of
295 the postsorption samples remains close to 100 Oe in all samples. This perturbation on the

296 magnetic properties of the materials under study could be related to the different corrosion
297 products from nZVI, which has less magnetic character than Fe⁰.

298 **3.2.Adsorption kinetics**

299 The effect of the contact time on the removal of Hg²⁺ and Pb²⁺ in single and
300 multicomponent systems was evaluated for the different materials by means of removal
301 kinetics. In the case of imogolite, an equilibrium time was achieved at 60 minutes for both
302 single- and multicomponent systems. For nZVI and Imo-nZVI, equilibrium was reached
303 after 30 minutes in all the studied systems (Fig. 3). Pb²⁺ removal was slightly higher than
304 Hg²⁺ removal in all the systems under study.

305 **3.3.PFO and PSO models**

306 Kinetic models of pseudo first order (PFO) and pseudo-second order (PSO) (Fig. 4) were
307 used to describe the kinetic behavior of the experimental data. The PFO model showed
308 the least adjustment of these data (Table 2). This behavior could be explained by the
309 theoretical fundamentals that differentiate both models. For example, in the case of the
310 PFO model, high levels of adjustment are observed when the analyte is monovalent,
311 which is removed by direct interaction between this species and a surface active site of
312 the substrate. For the PSO model, this condition occurs when an ion is attracted at two
313 active sites in the substrate. The removal of divalent cations is explained by this model,
314 favoring a chemical-type interaction (chemisorption), probably forming bidentate
315 complexes (Table 2).

316 The sorption capacities (q_e) of imogolite obtained from the PSO model (Eq. 5) for Pb²⁺
317 and Hg²⁺ were 44.9 and 39.4 mg·g⁻¹, respectively, in single-component systems.
318 However, as a result of the competition between cations, a reduction of more than 10%

319 was observed in the sorption capacity of imogolite in multicomponent systems. In the
320 case of nZVI, the removal of these metals was higher in both systems under study. This
321 is because this nanoparticle has multiple mechanisms of removal (adsorption,
322 precipitation, coprecipitation, and oxidation-reduction), unlike imogolite, for which
323 adsorption is the only mode of removal. The functionalization of imogolite with nZVI
324 improved the removal capacity of both Hg^{2+} and Pb^{2+} compared to the starting materials,
325 where the q_e values in the case of Pb^{2+} in single and multicomponent systems were 78.0
326 and $72.4 \text{ mg}\cdot\text{g}^{-1}$ and 81.0 and $77.7 \text{ mg}\cdot\text{g}^{-1}$, for Hg^{2+} , respectively. The removal rates of
327 both metals obtained from the PSO model (Eq. 5) show that the functionalization process
328 generates an increase in this parameter, which is up to 2.3 times greater than that observed
329 for imogolite and nZVI. The initial velocity (h), calculated from the PSO model, showed
330 that Pb^{2+} is removed by Imo-nZVI in early sorption stages compared to Hg^{2+} .

331 **3.4. Adsorption mechanisms**

332 The sorption mechanisms of Hg and Pb analytes in imogolite, nZVI and Imo-nZVI were
333 analyzed using the Elovich equation and Weber-Morris models (Fig. 5).

334 **Elovich equation**

335 The Elovich equation (Eq. 7) is a widely used model in various systems whose reactive
336 sites are energetically heterogeneous. The α parameter, associated with the initial rate of
337 adsorption, was higher in single-component systems for all the substrates studied,
338 indicating that the presence of both cations (Hg^{2+} and Pb^{2+}) generated a strong
339 competition for the active sites available in each material, explaining the lower values of
340 α in multicomponent systems (Table 3). The desorption constant obtained from this
341 model (β) was lower in the single-component systems, indicating that the different

342 available active sites can remove metals, observing the following decreasing order for
343 both metals Imo-nZVI > nZVI > imogolite (Fig. 5). However, in competition, this
344 parameter increases, showing that the removal of these analytes occurs in sites of greater
345 specificity.

346 **Intraparticle diffusion kinetic model**

347 As previously discussed (Table 3), the immobilization of nZVI in imogolite generated
348 changes in textural properties, which could generate changes in the overall removal rate
349 of Hg^{2+} and Pb^{2+} . The data were adjusted using the Weber-Morris model (Eq. 8) to
350 determine these changes and whether intraparticle diffusion is the limiting step of the
351 global speed for the removal process (Table 3). In general, multilinearity was observed
352 for all the systems under study. Reductive precipitation and surface sorption are the main
353 removal mechanism, with percentages greater than 90% (q_{e-1} values) of the analytes in all
354 the systems evaluated (Fig. 5), which is consequence of new sites of adsorption (Fe-OH
355 and Fe-O-OH) that provides the surface-functionalized imogolite with nZVI. C is related
356 to the thickness of the limiting layer associated with instantaneous adsorption. This
357 parameter was lower in multicomponent systems, which implies that accessibility to the
358 active sites where sorption occurs is dependent on the composition of the solution,
359 showing higher values for Hg. This result could be associated with the chemical
360 characteristics of this element (*i.e.*, ionic radius, polarizability, and electronegativity).

361 **Isotherm sorption**

362 The isotherms were studied for all elements in the single and multicomponent systems
363 (Fig. 6, Table 4) at pH 4.0, considering a range of concentrations of Hg^{2+} and Pb^{2+}
364 between 1 and 50 $\text{mg}\cdot\text{L}^{-1}$. In general, the curves of the isotherms showed an "L"-type
365 shape, which indicates good affinity between the substrate and the analytes, as well as a

366 greater removal capacity in the single-component systems. However, in nZVI and the
367 nanocomposite, the removal was greater than that in imogolite because in both substrates,
368 the interactions are favored due to the displacement of the IEP and decrease in ZP. The
369 experimental data were adjusted using the Langmuir model (Eq. 9), where q_{\max}
370 corresponds to the maximum removal capacity ($\text{mg} \cdot \text{g}^{-1}$) and K_L is the Langmuir constant
371 associated with the removal capacity ($\text{L} \cdot \text{mg}^{-1}$).

372 All the materials in the single and multicomponent systems showed higher values of q_{\max}
373 and K_L for Pb^{2+} than for Hg^{2+} . The values of q_{\max} for Pb^{2+} and Hg^{2+} in the single and
374 multicomponent systems had the same descending sequence: Imo-nZVI > nZVI >
375 Imogolite. Regarding the adsorption intensity (K_L), the nanocomposite showed an
376 increase in this parameter, reaching 1.2 and 1.4 times higher values in comparison to
377 nZVI and imogolite, respectively, probably associated with the decrease in the size of
378 nZVI immobilized on the surface of imogolite (Table 4).

379 According to Misono softness parameters ($Y_{\text{Hg}^{2+}}=4.24$ y $Y_{\text{Pb}^{2+}}=3.58$) (Misono et al.
380 1967), the functional groups of nZVI favored a stronger interaction with Hg^{2+} than Pb^{2+} ,
381 due to the fact that Fe has a borderline character on the Misono softness scale. This
382 observation is in agreement with the K_L value, which is a measure of the metal ion affinity
383 to the adsorption sites on materials, which is enhanced in multicomponent systems (Table
384 4). The free energy (ΔG°) was determined for each material in the systems under study at
385 a temperature of 25 °C and pH = 4.0 through the following equation: $\Delta G^\circ = -RT \ln K$,
386 where R is the gas constant ($8.134 \text{ J mol}^{-1} \cdot \text{K}^{-1}$) and T the temperature (K) using the
387 Langmuir isotherms (Table S1). However, Zhou & Zhou (2014) reported that K_L cannot
388 be used directly to obtain this parameter because it is expressed as $\text{L} \cdot \text{mg}^{-1}$. The standard
389 equilibrium constant (K°) using the Langmuir equation was calculated to avoid this
390 problem using the equation $K^\circ = K_L \cdot 10^3 \cdot 55.5$ and replaced in the Gibbs free energy

391 equation. The data obtained from this equation determined negative values of ΔG° for the
392 removal of Pb^{2+} and Hg^{2+} for imogolite, nZVI and the nanocomposite, both for single and
393 multicomponent systems (Table S1). Hence, the process of removing Pb^{2+} and Hg^{2+} is
394 spontaneous and thermodynamically favorable.

395 **Role of imogolite as a support for nZVI and its effects on the removal of Pb^{2+} and**
396 **Hg^{2+} .**

397 The structural and surface characteristics of imogolite describe how this nanotubular
398 aluminosilicate significantly favors the removal of neurotoxic metals, such as Pb^{2+} and
399 Hg^{2+} , in single and multicomponent systems when it is used as a support for nZVI. Several
400 investigations have shown that in situ synthesis of nZVI in different substrates, such as
401 activated carbon, zeolite, kaolinite, and montmorillonite, causes a decrease in size and
402 increase the removal capacity of nZVI; however, the impact of this process in imogolite
403 has important nuances to take into account:

404 Due to the variable charge of imogolite, which is positive with ZP values higher than 25
405 mV between pH 3 and 7, the formation of nZVI occurs mainly at the edges of the
406 nanotube, indicating that the surface sites have higher sensitivity to changes in pH, which
407 are neutral or negatively charged according to the synthesis conditions of nZVI, favoring
408 the adsorption of Fe^{3+} and generating nuclei of attraction for other iron ions.

409 The high density and magnetic and hydrophilic properties of nZVI prevent it from being
410 suspended, leading to rapid agglomeration and oxidation in aqueous systems, reducing
411 the removal capacity of different analytes (Peng et al. 2018). In contrast, the behavior of
412 imogolite is opposite to that described for nZVI since it remains in a stable suspension,
413 even under conditions of unfavorable pH and ionic strength, due to its low density and

414 because water can structure itself in different ways in the pores of imogolite, which allows
415 the Imo-nZVI composite to be in suspension under conditions when nZVI is not.
416 Immobilization of nZVI on imogolite increases the reactivity of the material adding a new
417 type of surface active sites with functional groups such as $\equiv\text{Fe}^{\text{(II)}}\text{-OH}$, $\equiv\text{Fe}^{\text{(II)}}\text{-OOH}$,
418 $\equiv\text{Fe}^{\text{(III)}}\text{-OH}$, and $\equiv\text{Fe}^{\text{(III)}}\text{-OOH}$, generated through the oxidation of the nZVI. These
419 functional groups could preferentially react with Hg^{2+} or Pb^{2+} according to the softness
420 of the analytes and the polarizability of the Fe(II)/Fe(III) group. Thus, hard Pb^{2+} would
421 interact preferentially with more polarized $\equiv\text{Fe}^{\text{(III)}}\text{-OOH}$ and $\equiv\text{Fe}^{\text{(III)}}\text{-OH}$ groups whereas
422 softer Hg^{2+} would interact with $\equiv\text{Fe}^{\text{(II)}}\text{-OH}$ and $\equiv\text{Fe}^{\text{(II)}}\text{-OOH}$ groups (Fig. 7).

423 **Conclusions**

424 The hybrid nanomaterial (Imo-nZVI) synthesized in this work represents a very
425 interesting type of material because of its exceptional properties and potential use in a
426 wide range of application fields. The synergistic combination of both components was
427 efficiently tested as a sorbent material for neurotoxic metals removal. Based on the speeds
428 and removal capacities obtained, Pb^{2+} was preferably removed by all materials, even in
429 systems that coexisted with Hg^{2+} . The process of immobilizing nZVI in imogolite caused
430 an increase of the speed and removal capacity of both metals compared to the starting
431 materials because the nZVI present in the nanocomposite is smaller than free nZVI. The
432 PSO and Langmuir models showed a better adjustment of the experimental data for all
433 the cases under study, which suggests that the removal process is produced by
434 chemisorption. The free energy associated with the removal of Pb^{2+} and Hg^{2+} indicates
435 that this process is spontaneous in all materials and is more favorable in nZVI. The
436 excellent percentage of recovery for Pb^{2+} and Hg^{2+} from water matrices and the magnetic
437 properties of Imo-nZVI make it a promising material for environmental applications.

438

439 **Declarations**

440 *Ethics approval and consent to participate*

441 *Not applicable*

442 *Consent for publication*

443 *Not applicable*

444 *Availability of data and materials*

445 *Not applicable*

446 *Competing interests*

447 *The authors declare that they have no competing interests*

448 **Funding**

449 *This work was supported by Consejo Nacional de Investigaciones Científicas y Técnicas*

450 *(CONICET), Agencia Nacional de Promoción Científica y Tecnológica (FONCYT)*

451 *(PICT-BID), Universidad Nacional de Cuyo (Argentina), Financiamiento Basal para*

452 *Centros Científicos y Tecnológicos de Excelencia AFB180001, Fondecyt Regular*

453 *1191018, PAI 77190014 and REDES 170170. CONICYT-PFCHA/Doctorado*

454 *Nacional/2019-21191242. ANID/CONICYT Postdoctoral FONDECYT N° 3180488*

455 **Authors' contributions**

456 *All authors contributed to the study conception and design. Material preparation, data*

457 *collection and analysis were performed by Estefanía M. Martinis and Nicolás Arancibia-*

458 *Miranda. Material characterization and sorption kinetic data analysis were performed*

459 *by Juliano C. Denardin, Raul Calderón, Cristóbal Flores, Karen Manquián-Cerdae and*

460 *Tamara Maldonadoe. The first draft of the manuscript was written by Estefania M.*

461 *Martinis and Nicolás Arancibia-Miranda. and all authors commented on previous*

462 *versions of the manuscript. All authors read and approved the final manuscript.*

463 **Acknowledgements**

464 *Consejo Nacional de Investigaciones Científicas y Técnicas (CONICET), Agencia*
465 *Nacional de Promoción Científica y Tecnológica (FONCYT) (PICT-BID), Universidad*
466 *Nacional de Cuyo (Argentina), Financiamiento Basal para Centros Científicos y*
467 *Tecnológicos de Excelencia AFB180001, Fondecyt Regular 1191018, PAI 77190014 and*
468 *REDES 170170. C.F. acknowledges CONICYT-PFCHA/Doctorado Nacional/2019-*
469 *21191242. T.M. acknowledges ANID/CONICYT Postdoctoral FONDECYT N° 3180488.*
470

471 **References**

- 472 Arancibia-Miranda N, Escudey M, Molina M, García-González MT (2011): Use of
473 isoelectric point and pH to evaluate the synthesis of a nanotubular aluminosilicate.
474 *J. Non-Cryst. Solids* 357, 1750-1756,
475 <https://doi.org/10.1016/j.jnoncrysol.2011.01.012>
- 476 Arancibia-Miranda N, Escudey M, Molina M, García-González MT (2013a): Kinetic and
477 surface study of single-walled aluminosilicate nanotubes and their precursors.
478 *Nanomaterials* 3, 126-140, <https://doi.org/10.3390/nano3010126>
- 479 Arancibia-Miranda N, Lillo S, Escudey M (2013b): Nanotubular aluminosilicates: a case
480 study for science and industry. *J. Chil. Chem. Soc.* 58, 2061-2066,
481 <https://doi.org/10.4067/S0717-97072013000400035>
- 482 Arancibia-Miranda N, Silva-Yumi J, Escudey M (2015): Effect of cations in the
483 background electrolyte on the adsorption kinetics of copper and cadmium and the
484 isoelectric point of imogolite. *J. Hazard. Mater.* 299, 675-684,
485 <https://doi.org/10.1016/j.jhazmat.2015.08.007>
- 486 Arancibia-Miranda N, Baltazar SE, García A, Muñoz-Lira D, Sepúlveda P, Rubio MA,
487 Altbir D (2016): Nanoscale zero valent supported by Zeolite and Montmorillonite:
488 Template effect of the removal of lead ion from an aqueous solution. *J. Hazard.*
489 *Mater.* 301, 371-380, <https://doi.org/10.1016/j.jhazmat.2015.09.007>
- 490 Arancibia-Miranda N, Manquían-Cerda K, Pizarro C, Maldonado T, Suazo-Hernández J,
491 Escudey M, Bolan N, Sarkar B (2020): Mechanistic insights into simultaneous
492 removal of copper, cadmium and arsenic from water by iron oxide-functionalized
493 magnetic imogolite nanocomposites. *J. Hazard. Mater.* 398, 122940,
494 <https://doi.org/10.1016/j.jhazmat.2020.122940>
- 495 Arancibia-Miranda Ns, Escudey M, Ramírez R, González RI, Van Duin AC, Kiwi M
496 (2017): Advancements in the synthesis of building block materials: experimental
497 evidence and modeled interpretations of the effect of Na and K on imogolite
498 synthesis. *J. Phys. Chem. B* 121, 12658-12668,
499 <https://doi.org/10.1021/acs.jpcc.6b12155>
- 500 Baltazar SE, García A, Romero AH, Rubio MA, Arancibia-Miranda N, Altbir D (2014):
501 Surface rearrangement of nanoscale zerovalent iron: the role of pH and its
502 implications in the kinetics of arsenate sorption. *Environ. Technol.* 35, 2365-2372,
503 <https://doi.org/10.1080/09593330.2014.904932>
- 504 Bonelli B (2016): Surface chemical modifications of imogolite, *Developments in Clay*
505 *Science*. Elsevier, pp. 279-307
- 506 Boparai HK, Joseph M, O'Carroll DM (2011): Kinetics and thermodynamics of cadmium
507 ion removal by adsorption onto nano zerovalent iron particles. *J. Hazard. Mater.*
508 186, 458-465, <https://doi.org/10.1016/j.jhazmat.2010.11.029>
- 509 Bossa N, Carpenter AW, Kumar N, de Lannoy C-F, Wiesner M (2017): Cellulose
510 nanocrystal zero-valent iron nanocomposites for groundwater remediation.
511 *Environ. Sci. Nano* 4, 1294-1303, <https://doi.org/10.1039/C6EN00572A>
- 512 Cáceres-Jensen L, Rodríguez-Becerra J, Parra-Rivero J, Escudey M, Barrientos L,
513 Castro-Castillo V (2013): Sorption kinetics of diuron on volcanic ash derived soils.
514 *J. Hazard. Mater.* 261, 602-613, <https://doi.org/10.1016/j.jhazmat.2013.07.073>
- 515 Cradwick P, Farmer V, Russell J, Masson C, Wada K, Yoshinaga N (1972): Imogolite, a
516 hydrated aluminium silicate of tubular structure. *Nat. Phys. Sci.* 240, 187-189,
517 <https://doi.org/10.1038/physci240187a0>

- 518 Crane R, Scott T (2012): Nanoscale zero-valent iron: future prospects for an emerging
519 water treatment technology. *J. Hazard. Mater.* 211, 112-125,
520 <https://doi.org/10.1016/j.jhazmat.2011.11.073>
- 521 Charlet L, Chapron Y, Faller P, Kirsch R, Stone AT, Baveye PC (2012):
522 Neurodegenerative diseases and exposure to the environmental metals Mn, Pb,
523 and Hg. *Coord. Chem. Rev.* 256, 2147-2163,
524 <https://doi.org/10.1016/j.ccr.2012.05.012>
- 525 Cheung W, Szeto Y, McKay G (2007): Intraparticle diffusion processes during acid dye
526 adsorption onto chitosan. *Bioresour. Technol.* 98, 2897-2904,
527 <https://doi.org/10.1016/j.biortech.2006.09.045>
- 528 Chien S, Clayton W (1980): Application of Elovich equation to the kinetics of phosphate
529 release and sorption in soils. *Soil Sci. Soc. Am. J.* 44, 265-268,
530 <https://doi.org/10.2136/sssaj1980.03615995004400020013x>
- 531 Dror I, Jacov OM, Cortis A, Berkowitz B (2012): Catalytic transformation of persistent
532 contaminants using a new composite material based on nanosized zero-valent iron.
533 *ACS Appl. Mater. Inter.* 4, 3416-3423, <https://doi.org/10.1021/am300402q>
- 534 Ho Y-S, McKay G (2000): The kinetics of sorption of divalent metal ions onto sphagnum
535 moss peat. *Water Res.* 34, 735-742, [https://doi.org/10.1016/S0043-1354\(99\)00232-8](https://doi.org/10.1016/S0043-1354(99)00232-8)
- 537 Jaishankar M, Tseten T, Anbalagan N, Mathew BB, Beeregowda KN (2014): Toxicity,
538 mechanism and health effects of some heavy metals. *Interdiscip. Toxicol.* 7, 60-
539 72, <https://doi.org/10.2478/intox-2014-0009>
- 540 Jiang D, Zeng G, Huang D, Chen M, Zhang C, Huang C, Wan J (2018): Remediation of
541 contaminated soils by enhanced nanoscale zero valent iron. *Environ. Res.* 163,
542 217-227, <https://doi.org/10.1016/j.envres.2018.01.030>
- 543 Kanel SR, Manning B, Charlet L, Choi H (2005): Removal of arsenic (III) from
544 groundwater by nanoscale zero-valent iron. *Environ. Sci. Technol.* 39, 1291-1298,
545 <https://doi.org/10.1021/es048991u>
- 546 Kang D-Y, Brunelli NA, Yucelen GI, Venkatasubramanian A, Zang J, Leisen J, Hesketh
547 PJ, Jones CW, Nair S (2014): Direct synthesis of single-walled
548 aminoaluminosilicate nanotubes with enhanced molecular adsorption selectivity.
549 *Nat. Commun.* 5, 1-9, <https://doi.org/10.1038/ncomms4342>
- 550 Kim SA, Kamala-Kannan S, Lee K-J, Park Y-J, Shea PJ, Lee W-H, Kim H-M, Oh B-T
551 (2013): Removal of Pb (II) from aqueous solution by a zeolite–nanoscale zero-
552 valent iron composite. *Chem. Eng. J.* 217, 54-60,
553 <https://doi.org/10.1016/j.cej.2012.11.097>
- 554 Lagergren S (2013): Zur theorie der sogenannten adsorption gelöster stoffe,
555 *KungligaSvenska Vetenskapsakademiens. Handlingar* 24: 1–39
- 556 Levard C, Doelsch E, Rose J, Masion A, Basile-Doelsch I, Proux O, Hazemann J-L,
557 Borschneck D, Bottero J-Y (2009): Role of natural nanoparticles on the speciation
558 of Ni in andosols of la Reunion. *Geochim. Cosmochim. Acta* 73, 4750-4760,
559 <https://doi.org/10.1016/j.gca.2009.05.053>
- 560 Li X-q, Elliott DW, Zhang W-x (2006): Zero-valent iron nanoparticles for abatement of
561 environmental pollutants: materials and engineering aspects. *Crit. Rev. Solid State*
562 *Mater. Sci.* 31, 111-122, <https://doi.org/10.1080/10408430601057611>
- 563 Lu HJ, Wang JK, Ferguson S, Wang T, Bao Y, Hao HX (2016): Mechanism, synthesis
564 and modification of nano zerovalent iron in water treatment. *Nanoscale* 8, 9962-
565 9975, <https://doi.org/10.1039/c6nr00740f>
- 566 Manquián-Cerda K, Cruces E, Rubio MA, Reyes C, Arancibia-Miranda N (2017):
567 Preparation of nanoscale iron (oxide, oxyhydroxides and zero-valent) particles

568 derived from blueberries: reactivity, characterization and removal mechanism of
569 arsenate. *Ecotox. Environ. Safe.* 145, 69-77,
570 <https://doi.org/10.1016/j.ecoenv.2017.07.004>

571 Misono M, Ochiai Ei, Saito Y, Yoneda Y (1967): A new dual parameter scale for the
572 strength of Lewis acids and bases with the evaluation of their softness. *J. Inorg.*
573 *Nucl. Chem.* 29, 2685-2691, [https://doi.org/10.1016/0022-1902\(67\)80006-X](https://doi.org/10.1016/0022-1902(67)80006-X)

574 Noubactep C (2008): A critical review on the process of contaminant removal in Fe⁰-
575 H₂O systems. *Environ. Technol.* 29, 909-920,
576 <https://doi.org/10.1080/09593330802131602>

577 Peng Z, Xiong C, Wang W, Tan F, Wang X, Qiao X, Wong PK (2018): Hydrophobic
578 modification of nanoscale zero-valent iron with excellent stability and floatability
579 for efficient removal of floating oil on water. *Chemosphere* 201, 110-118,
580 <https://doi.org/j.chemosphere.2018.02.149>

581 Rao CNR, Müller A, Cheetham AK (2006): The chemistry of nanomaterials: synthesis,
582 properties and applications. John Wiley & Sons

583 Rudzinski W, Panczyk T (2000): Kinetics of isothermal adsorption on energetically
584 heterogeneous solid surfaces: a new theoretical description based on the statistical
585 rate theory of interfacial transport. *J. Phys. Chem. B* 104, 9149-9162,
586 <https://doi.org/10.1021/jp000045m>

587 Rudzinski W, Plazinski W (2008): Kinetics of solute adsorption at solid/aqueous
588 interfaces: searching for the theoretical background of the modified pseudo-first-
589 order kinetic equation. *Langmuir* 24, 5393-5399,
590 <https://doi.org/10.1021/la8000448>

591 Shi Z, Nurmi JT, Tratnyek PG (2011): Effects of nano zero-valent iron on oxidation-
592 reduction potential. *Environ. Sci. Technol.* 45, 1586-1592,
593 <https://doi.org/10.1021/es103185t>

594 Sposito G (1989): *Chemistry of Soils*. New York: Oxford University Pres. Inc, pp. 277

595 Stefaniuk M, Oleszczuk P, Ok YS (2016): Review on nano zerovalent iron (nZVI): from
596 synthesis to environmental applications. *Chem. Eng. J.* 287, 618-632,
597 <https://doi.org/10.1016/j.cej.2015.11.046>

598 Suazo-Hernández J, Sepúlveda P, Manquián-Cerda K, Ramírez-Tagle R, Rubio MA,
599 Bolan N, Sarkar B, Arancibia-Miranda N (2019): Synthesis and characterization
600 of zeolite-based composites functionalized with nanoscale zero-valent iron for
601 removing arsenic in the presence of selenium from water. *J. Hazard. Mater.* 373,
602 810-819, <https://doi.org/10.1016/j.jhazmat.2019.03.125>

603 Suazo-Hernández J, Manquián-Cerda K, de la Luz Mora M, Molina-Roco M, Rubio MA,
604 Sarkar B, Bolan N, Arancibia-Miranda N (2020): Efficient and selective removal
605 of SeVI and AsV mixed contaminants from aqueous media by montmorillonite-
606 nanoscale zero valent iron nanocomposite. *J. Hazard. Mater.* 403, 123639,
607 <https://doi.org/10.1016/j.jhazmat.2020.123639>

608 Weber WJ, Morris JC (1963): Kinetics of adsorption on carbon from solution. *J. Sanit.*
609 *Eng. Div.* 89, 31-60, <https://doi.org/10.1061/JSEDAI.0000430>

610 Wu F-C, Tseng R-L, Juang R-S (2001): Kinetic modeling of liquid-phase adsorption of
611 reactive dyes and metal ions on chitosan. *Water Res.* 35, 613-618,
612 [https://doi.org/10.1016/S0043-1354\(00\)00307-9](https://doi.org/10.1016/S0043-1354(00)00307-9)

613 Wu F-C, Tseng R-L, Juang R-S (2009): Characteristics of Elovich equation used for the
614 analysis of adsorption kinetics in dye-chitosan systems. *Chem. Eng. J.* 150, 366-
615 373, <https://doi.org/10.1016/j.cej.2009.01.014>

616 Yan W, Herzing AA, Kiely CJ, Zhang W-x (2010): Nanoscale zero-valent iron (nZVI):
617 aspects of the core-shell structure and reactions with inorganic species in water. J.
618 Contam. Hydrol. 118, 96-104, <https://doi.org/10.1016/j.jconhyd.2010.09.003>
619 Zhang X, Lin S, Chen Z, Megharaj M, Naidu R (2011): Kaolinite-supported nanoscale
620 zero-valent iron for removal of Pb²⁺ from aqueous solution: reactivity,
621 characterization and mechanism. Water Res. 45, 3481-3488,
622 <https://doi.org/10.1016/j.watres.2011.04.010>
623 Zou Y, Wang X, Khan A, Wang P, Liu Y, Alsaedi A, Hayat T, Wang X (2016):
624 Environmental remediation and application of nanoscale zero-valent iron and its
625 composites for the removal of heavy metal ions: a review. Environ. Sci. Technol.
626 50, 7290-7304, <https://doi.org/10.1021/acs.est.6b01897>
627

628 **Figure Captions**

629 **Fig. 1.** Morphology of the samples obtained by HR-TEM.

630 **Fig. 2.** ZP vs. pH plot of synthetic Imo, nZVI, and Imo-nZVI.

631 **Fig. 3.** Effect of contact time on the removal of heavy metals from each sample.

632 **Fig. 4.** Kinetic models of pseudo first-order (PFO) for (a) Imo, (b) nZVI, and (c) Imo-
633 nZVI and pseudo second-order (PSO) for (d) Imo, (e) nZVI, and (f) Imo-nZVI.

634 **Fig. 5.** Fits of the experimental data to the Elovich equation for (a) imogolite, (b) nZVI,
635 and (c) Imo-nZVI and Weber-Morris model for (d) Imo, (e) nZVI, and (f) Imo-nZVI.

636 **Fig. 6.** Langmuir isotherm for the adsorption of Pb^{2+} and Hg^{2+} in single (S) and
637 multicomponent (M) systems on nZVI, Imo, and Imo-nZVI.

638 **Fig. 7.** Schematic representation of the possible interactions that occur on the surface of
639 the Imo-nZVI. The affinity and intensity of removal of Pb^{2+} and Hg^{2+} with the different
640 groups of the nanocomposite is conditioned by the magnitude of the Misono softness
641 parameters ($Y_{Hg^{2+}} = 4.24$ and $Y_{Pb^{2+}} = 3.58$) and the possibility they have of interacting
642 with functional groups with similar characteristics.

643

644

645

646

647

648 Fig. 1

649

650

651

652

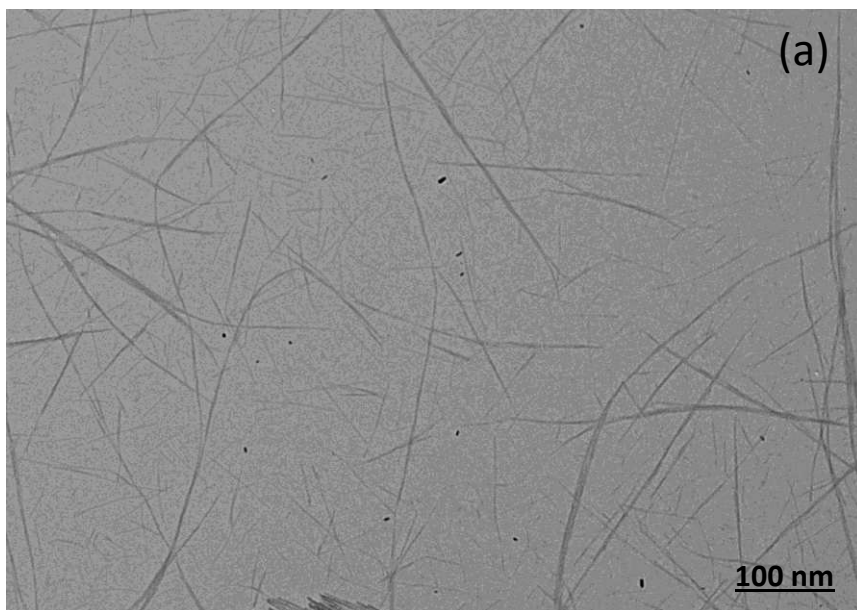
653

654

655

656

657



658

659

660

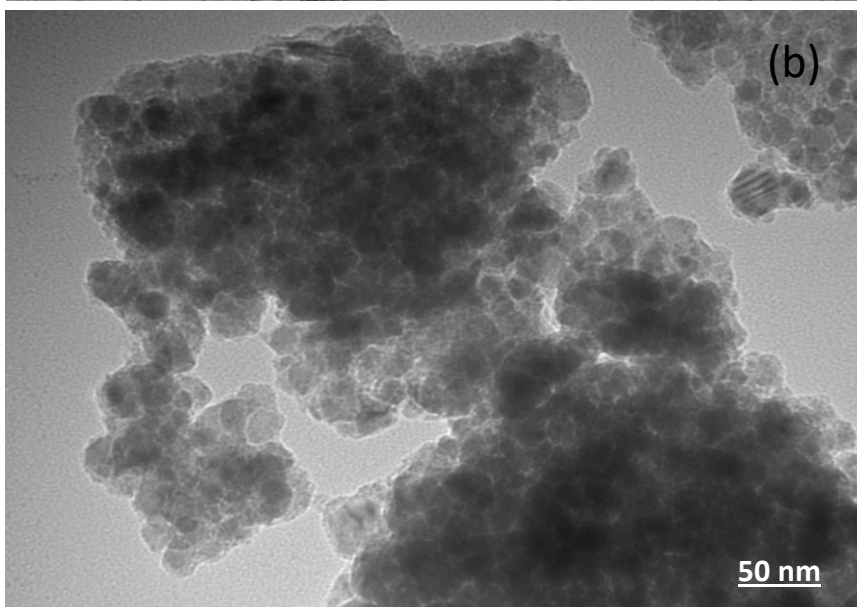
661

662

663

664

665



666

667

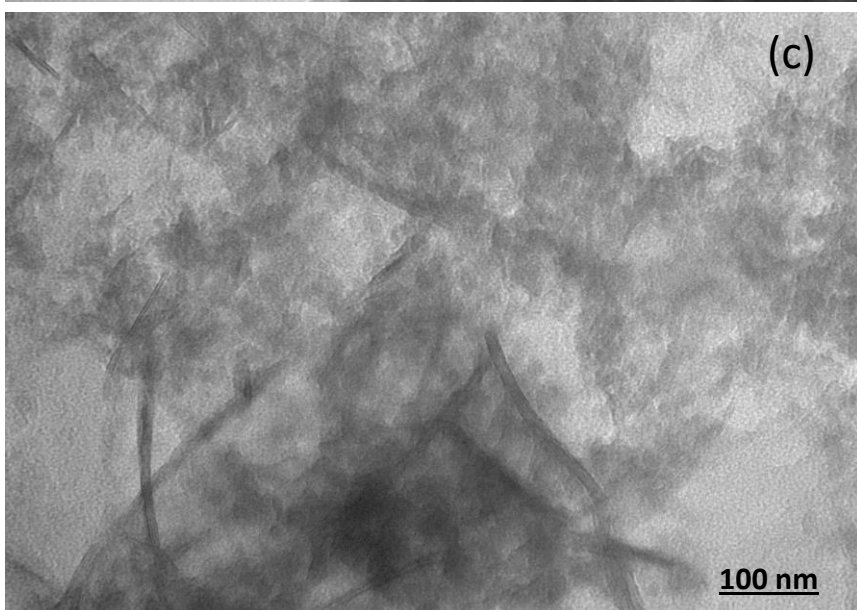
668

669

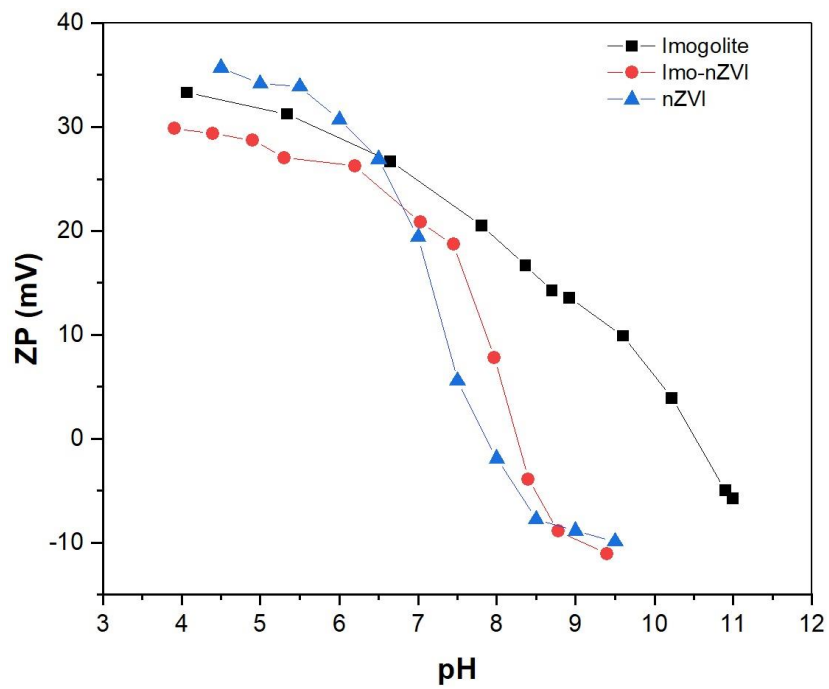
670

671

672



673 Fig. 2



674

675

676

677

678

679

680

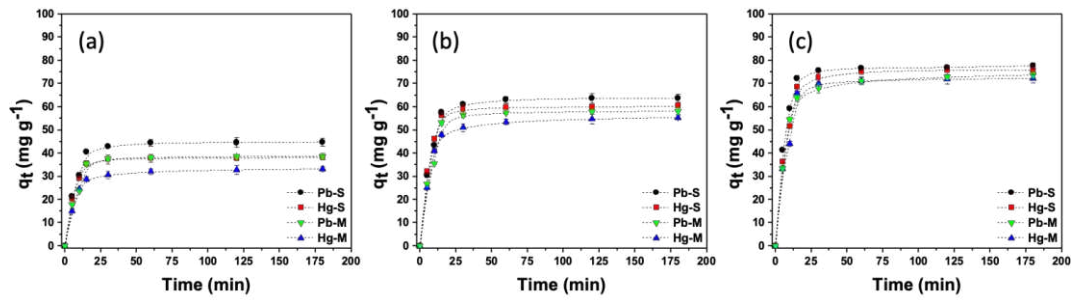
681

682

683

684

685 Fig. 3



686

687

688

689

690

691

692

693

694

695

696

697

698

699

700

701

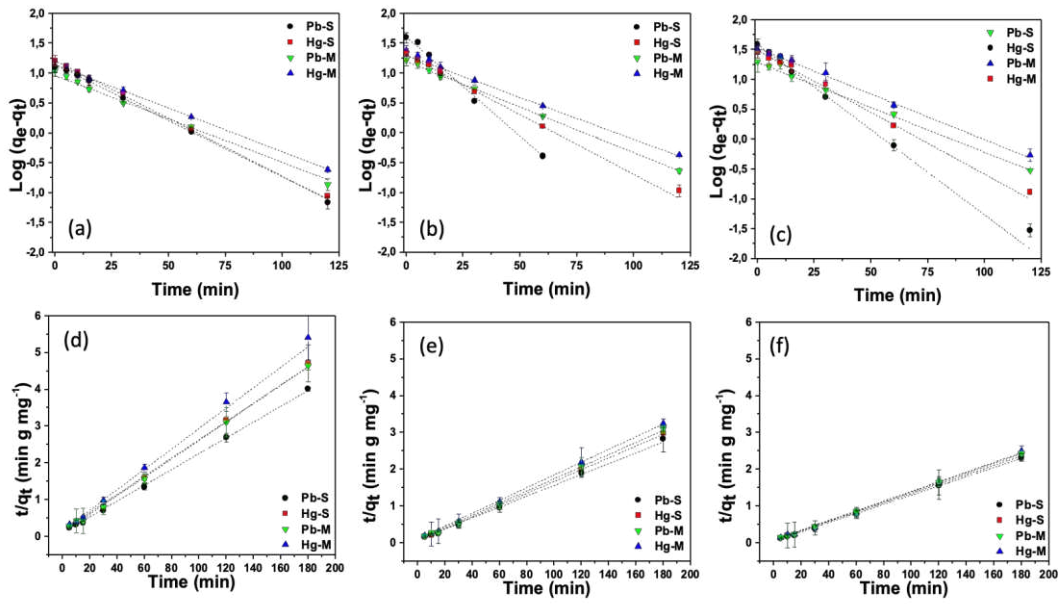
702

703

704

705

706 Fig. 4



707

708

709

710

711

712

713

714

715

716

717

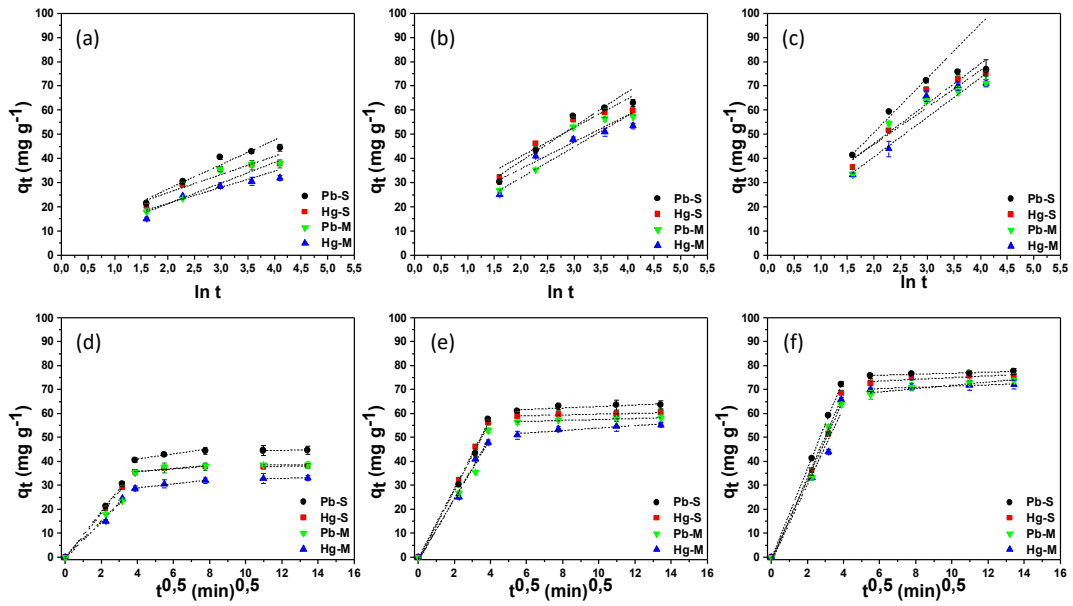
718

719

720

721

722



724

725

726

727

728

729

730

731

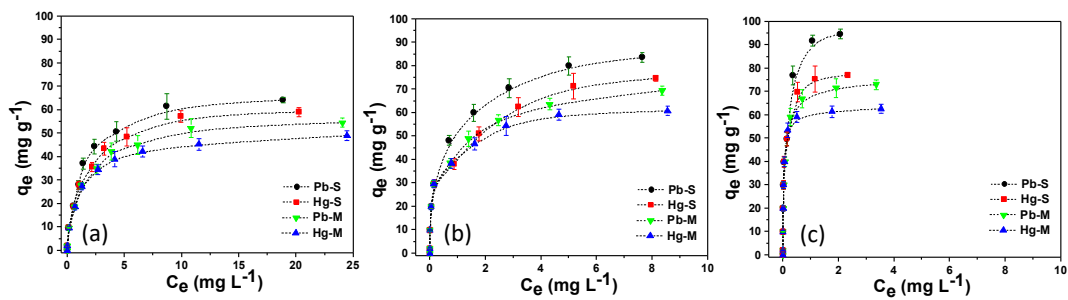
732

733

734

735

736 Fig. 6



737

738

739

740

741

742

743

744

745

746

747

748

749

750

751

752

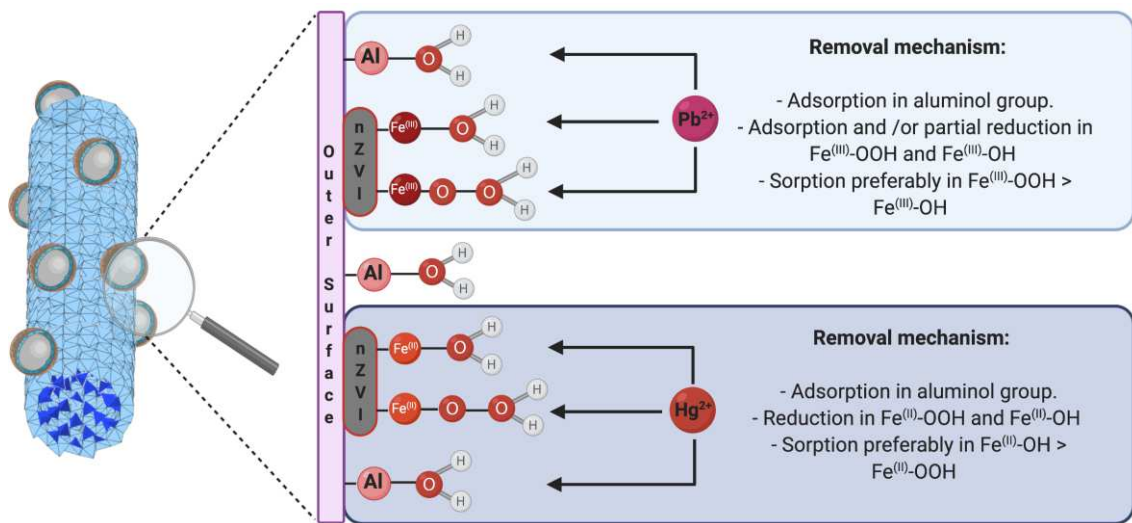
753

754

755

756

757 Fig. 7



758

759

760

761

762

763

764

765

766

767

768

769

770

771

772

773

774

775

776 **Table 1.** Specific surface area and porosity parameters of imogolite, nZVI and Imo-nZVI.

Parameters	Imogolite	nZVI	Imo-nZVI
Specific surface area (m ² ·g ⁻¹)	310	87	234
External surface area (m ² ·g ⁻¹)	180	35	133
Micropore volume x10 ⁻³ (cm ³ ·g ⁻¹)	20	1.5	26
Micropore area (m ² ·g ⁻¹)	66	17	50
Pore Volume (cm ³ ·g ⁻¹)	0.25	0.18	0.22
Pore diameter (Å)	10	18	13

777

778

779

780

781

782

783

784

785

786

787

788

789

790

791

792 **Table 2.** Kinetic parameters predicted from pseudo first and pseudo second-order
 793 models. Standard error for each parameter is included in parenthesis.

Parameters	Pb ²⁺ (single component)			Pb ²⁺ (multi component)		
	Imogolite	nZVI	Imo-nZVI	Imogolite	nZVI	Imo-nZVI
q_{exp} (mg·g⁻¹)	44.84 (3.26)	63.66 (6.12)	77.67 (6.89)	38.75(3.42)	58.14 (5.55)	73.70 (6.99)
q_{exp} (%)	49.82 (3.33)	70.73 (7.16)	86.30 (7.99)	43.06 (4.29)	64.60 (6.07)	81.89 (8.16)
<i>Pseudo-second Order</i>						
q_e (mg·g⁻¹)	47.90 (3.46)	68.01 (6.66)	81.96 (7.74)	41.68 (4.09)	62.54 (5.99)	77.43 (7.99)
k₂ x10⁻³(g·mg⁻¹·min⁻¹)	4.24 (0.26)	2.98 (0.12)	3.01 (0.41)	4.34 (0.29)	2.90 (0.11)	2.68 (0.31)
h (mg·g⁻¹·min⁻¹)	9.73	13.78	20.22	7.54	11.34	16.07
r²	0.972	0.977	0.987	0.969	0.983	0.977
Models	Hg ²⁺ (single component)			Hg ²⁺ (multi component)		
	Imogolite	nZVI	Imo-nZVI	Imogolite	nZVI	Imo-nZVI
q_{exp} (mg·g⁻¹)	38.25 (3.44)	60.41 (7.11)	75.83 (6.95)	33.24 (3.81)	55.41 (5.26)	72.20 (8.01)
q_{exp} (%)	42.50 (3.98)	67.12 (6.14)	84.26 (7.33)	36.93 (3.06)	61.57 (5.17)	80.22 (7.94)
<i>Pseudo-second Order</i>						
q_e (mg·g⁻¹)	40.36 (4.46)	63.74 (6.53)	81.01 (8.03)	34.92 (3.80)	58.21 (5.11)	77.66 (7.26)
k₂ x10⁻³(g·mg⁻¹·min⁻¹)	6.54 (0.51)	4.14 (0.46)	2.50 (0.22)	5.95 (0.61)	3.57 (0.41)	2.33 (0.29)
h (mg·g⁻¹·min⁻¹)	10.65	16.82	16.41	7.26	12.10	14.05
r²	0.978	0.987	0.981	0.979	0.963	0.977

794

795

796

797

798

799 **Table 3.** Kinetic parameters predicted from the linear analysis of Elovich and intraparticle
800 diffusion kinetic models. Standard error for each parameter is included in parenthesis.

Elovich		Pb²⁺ (single-component)			Pb²⁺ (multi-component)		
Equation		Imogolite	nZVI	Imo-nZVI	Imogolite	nZVI	Imo-nZVI
α		9.09 (0.51)	16.39 (2.01)	18.94 (1.71)	8.50 (1.10)	11.54 (0.83)	11.99 (1.21)
β		0.06 (0.00)	0.07 (0.01)	0.07 (0.00)	0.06 (0.01)	0.07 (0.00)	0.10 (0.01)
RMSE		0.41	5.75	0.51	18.00	1.03	11.58
r²		0.993	0.937	0.990	0.773	0.993	0.937
Elovich		Hg²⁺ (single-component)			Hg²⁺ (multi-component)		
Equation		Imogolite	nZVI	Imo-nZVI	Imogolite	nZVI	Imo-nZVI
α		16.94 (1.24)	18.84 (2.31)	24.35 (2.63)	13.64 (0.11)	14.17 (2.03)	19.52 (0.19)
		0.05 (0.00)	0.05 (0.01)	0.06 (0.00)	0.09 (0.00)	0.10 (0.02)	0.14 (0.00)
RMSE		1.41	40.51	16.43	1.70	62.46	2.49
r²		0.990	0.773	0.937	0.993	0.773	0.990
Intraparticles		Pb²⁺ (single-component)			Pb²⁺ (multi-component)		
Diffusion		Imogolite	nZVI	Imo-nZVI	Imogolite	nZVI	Imo-nZVI
q_{e1}		28.84 (3.23)	48.18 (3.99)	66.47 (7.99)	36.30 (4.01)	58.84 (5.29)	69.00 (7.03)
k_{int1}		0.10 (0.02)	0.16 (0.02)	0.36 (0.05)	0.31 (0.02)	0.52 (0.04)	0.25 (0.03)
C₁		13.3 (1.20)	25.4 (1.99)	33.1 (4.29)	20.21 (2.54)	33.03 (3.54)	35.1 (3.43)
r²		0.951	0.951	0.857	0.950	0.950	0.954
Intraparticles		Hg²⁺ (single-component)			Hg²⁺ (multi-component)		
Diffusion		Imogolite	nZVI	Imo-nZVI	Imogolite	nZVI	Imo-nZVI
q_{e1}		34.29 (4.01)	52.00 (5.78)	74.82 (7.09)	41.04 (4.21)	58.57 (5.99)	73.96 (8.01)
k_{int1}		0.21 (0.01)	0.31 (0.04)	0.21 (0.01)	0.14 (0.05)	0.20 (0.01)	0.69 (0.01)
C₁		17.35 (2.23)	27.15 (2.27)	72.7 (5.99)	22.3 (3.01)	31.1 (3.02)	41.3 (4.12)
r²		0.859	0.856	0.951	0.864	0.954	0.950

801

802

803

804

805 **Table 4.** Parameters of Langmuir isotherm models for Pb²⁺ and Hg²⁺ adsorption on
 806 imogolite, nZVI and Imo-nZVI in single and multi-component systems. Standard error
 807 for each parameter is included in parenthesis.

Parameters	Pb ²⁺ (single-component)			Pb ²⁺ (multi-component)		
	Imogolite	nZVI	Imo-nZVI	Imogolite	nZVI	Imo-nZVI
q_{max}	68.84 (7.22)	81.43 (8.31)	94.77 (9.42)	62.75 (7.01)	70.65 (7.07)	76.94 (7.13)
K_L	0.77 (0.08)	2.92 (0.23)	16.66 (1.72)	0.73 (0.09)	2.78 (0.25)	31.50 (0.37)
r²	0.989	0.991	0.998	0.969	0.996	0.977

Parameters	Hg ²⁺ (single-component)			Hg ²⁺ (multi-component)		
	Imogolite	nZVI	Imo-nZVI	Imogolite	nZVI	Imo-nZVI
q_{max}	56.99 (5.92)	62.08 (6.61)	72.66 (7.22)	49.76 (7.22)	56.00 (7.22)	61.58 (7.22)
K_L	0.74 (0.07)	5.55 (0.48)	21.71 (3.01)	0.93 (0.11)	7.84 (0.80)	54.02 (5.98)
r²	0.990	0.993	0.979	0.974	0.996	0.987

808

809

810

811

812

813

814

815

816

817

818

819

820

821

822

823

824

Supporting information

825

Enhanced removal of mercury and lead by a novel and

826

efficient surface-functionalized imogolite with nanoscale zero-

827

valent iron material

828

Estefanía M. Martinis^{a*}, Juliano C. Denardin^b, Raul Calderón^{c,d}, Cristóbal Flores^e,

829

Karen Manquián-Cerda^e, Tamara Maldonado^e, Nicolás Arancibia-Miranda^{b,e*}

830

^aFacultad de Ingeniería, Universidad Nacional de Cuyo, Consejo Nacional de

831

Investigaciones Científicas y Técnicas, UNCUYO-CONICET, Mendoza, Argentina

832

^bCenter for the Development of Nanoscience and Nanotechnology, CEDENNA, Santiago,

833

Chile

834

^cCentro de Investigación en Recursos Naturales y Sustentabilidad, Universidad Bernardo

835

O'Higgins, Fabrica, 1990, Segundo Piso, Santiago, Chile

836

^dInstituto de Investigaciones Agropecuarias, INIA La Platina, Santa Rosa, 11610,

837

Santiago, Chile

838

^eFacultad de Química y Biología, Universidad de Santiago de Chile, Santiago, Chile

839

**Corresponding authors. Tel.: +56 2 7181048; fax: +56 2 27181048*

840

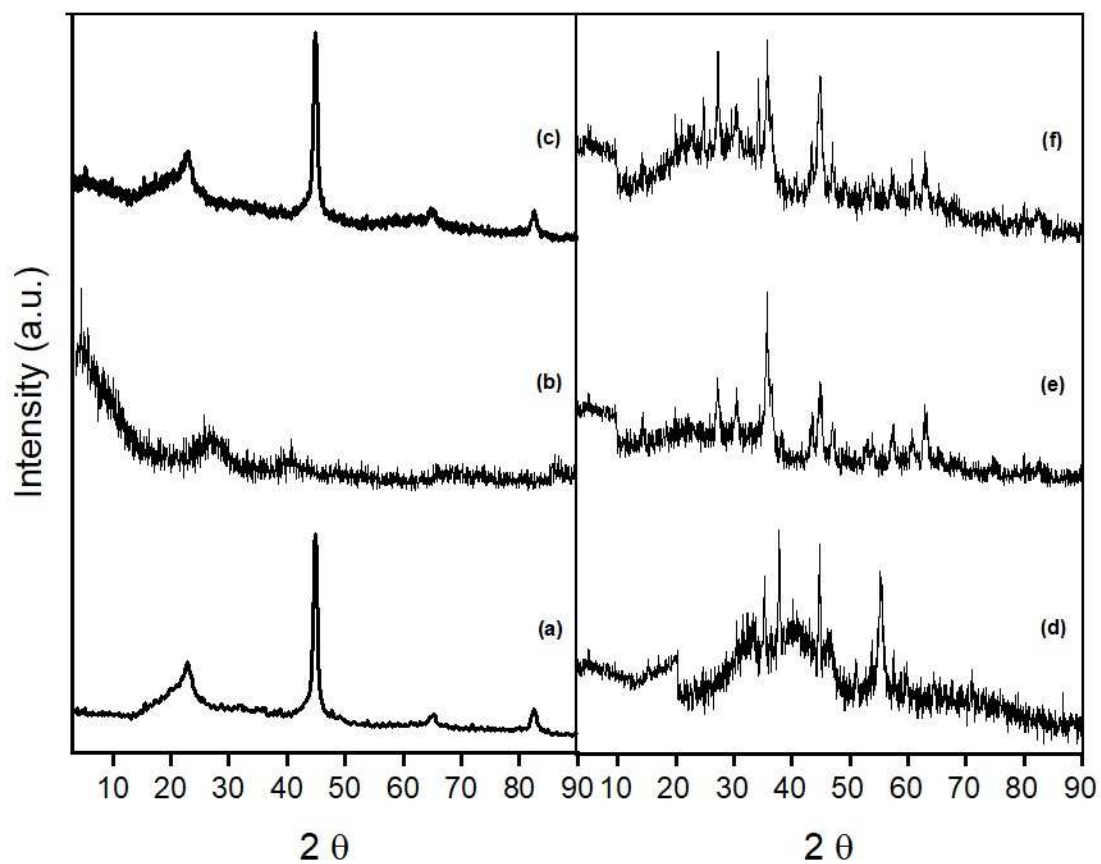
*E-mail address: **nicolas.arancibia@usach.cl** (N. Arancibia-Miranda)*

841

***emartinis@mendoza-conicet.gob.ar** (Estefanía M. Martinis)*

842

843



844

845 **Fig S1.** X-ray diffraction of imogolite (a), nZVI (b), Imo-nZVI (c), Imo-nZVI/Pb (d),

846 Imo-nZVI/Hg (e), and Imo-nZVI/Pb-Hg (f).

847

848

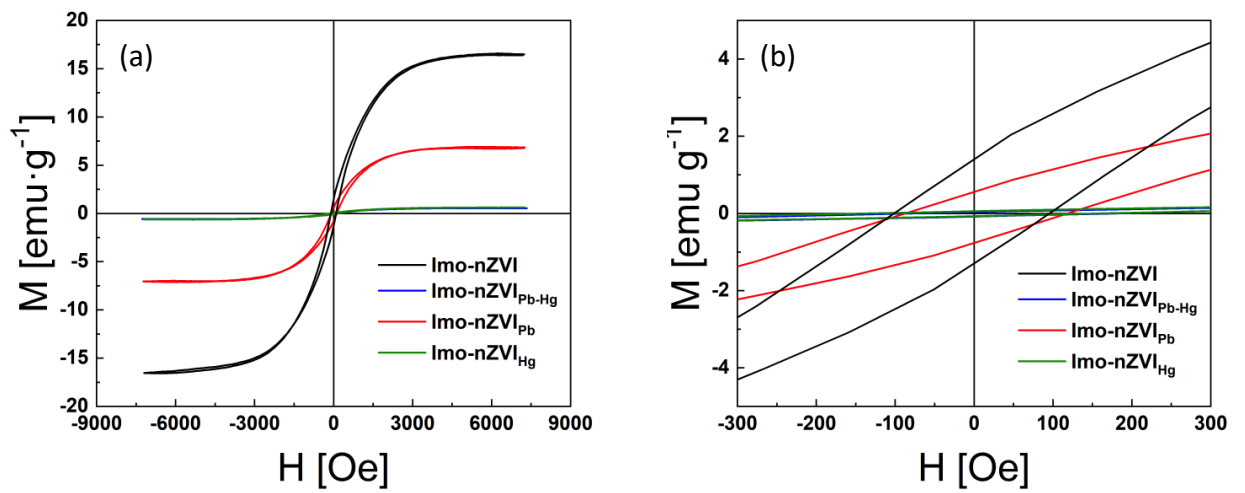
849

850

851

852

853



854

855 **Fig S2.** Hysteresis curve of Imo-nZVI pre- and post-sorption of Hg, Pb and Pb-Hg (a).

856 Enlargement of the magnetization curves (b).

857

858

859

860 **Table S1. Speciation curve**

Species	Log K	Conc. [mol/l]
Hg²⁺⁺	0.000E0	0,182
Hg^{2OH+}	-4900	0,00228
K⁺	0.000E0	9,93
KOH	-14500	3,13E-11
KNO₃	-150	0,0696
NO₃⁻	0.000E0	9,91
Pb⁺⁺	0.000E0	0,158
PbOH⁺	-7700	0,00000314
Pb(OH)₂	-17100	1,25E-12
Pb(OH)₃⁻	-28100	1,24E-20
Pb₂OH⁺⁺⁺	-6400	9,87E-09
Pb₃(OH)₄⁺⁺	-23900	4,89E-21
Pb₄(OH)₄⁺⁺⁺⁺	-20900	7,71E-22
Pb₆(OH)₈⁺⁺⁺⁺	-43600	3,79E-40
PbNO₃⁺	1170	0,0231
Pb(NO₃)₂	1400	0,000389
OH⁻	-14000	9,98E-09
H⁺	0.000E0	1

861

862

863

864

865

866

867 **Table S2. ΔG values for the studied materials.**

Parameters	Pb ²⁺ (single component)			Pb ²⁺ (multi component)		
	Imogolite	nZVI	Imo-nZVI	Imogolite	nZVI	Imo-nZVI
ΔG (J·mol ⁻¹)x10 ³	-45.2	-50.2	-54.5	-45.3	-48.6	-52.9

Parameters	Hg ²⁺ (single component)			Hg ²⁺ (multi component)		
	Imogolite	nZVI	Imo-nZVI	Imogolite	nZVI	Imo-nZVI
ΔG (J·mol ⁻¹) x10 ³	-45.7	-51.0	-55.8	-45.1	-48.4	-53.5

868

869

870

871

872

873

874

875

876

877

878

879

880

881

882

Figures

Fig. 1

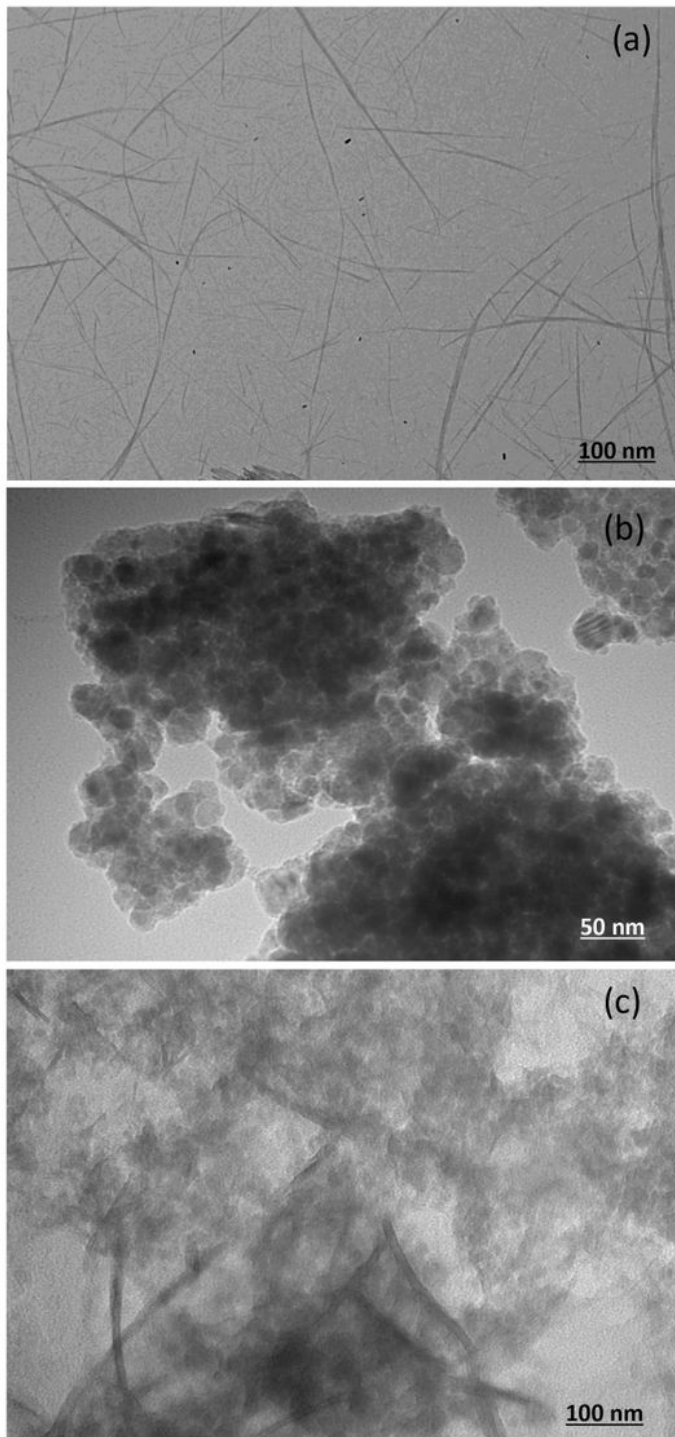


Figure 1

Morphology of the samples obtained by HR-TEM.

Fig. 2

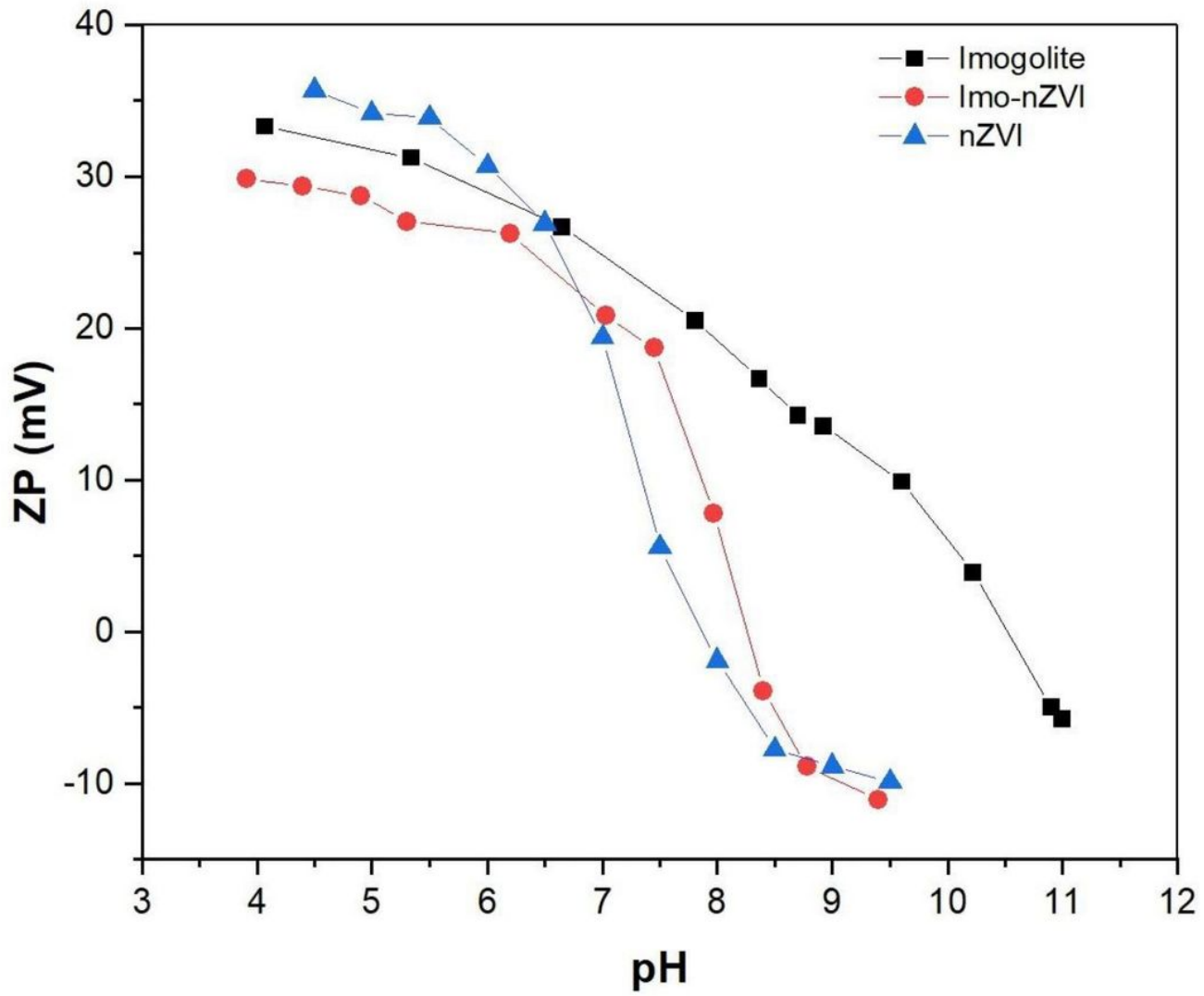


Figure 2

ZP vs. pH plot of synthetic Imo, nZVI, and Imo-nZVI.

Fig. 3

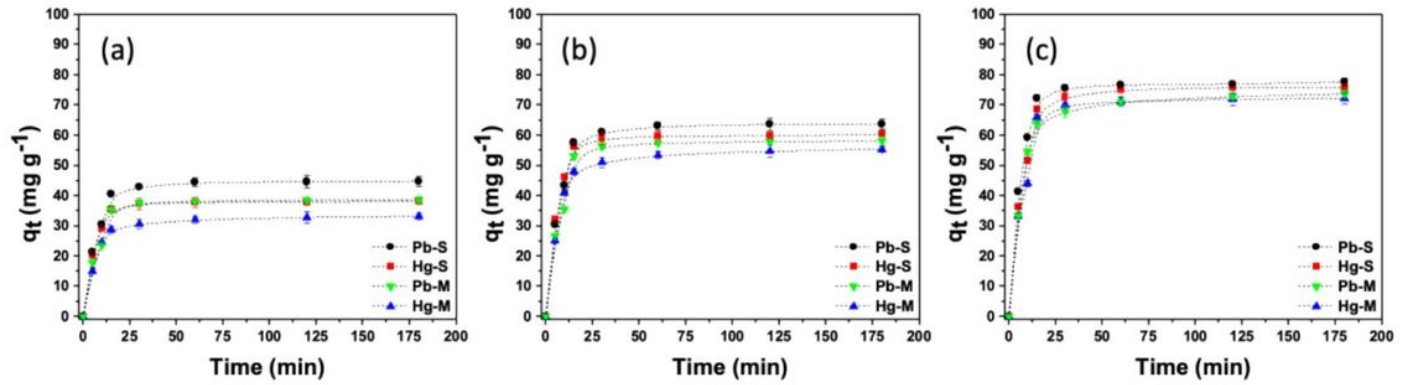


Figure 3

Effect of contact time on the removal of heavy metals from each sample.

Fig. 4

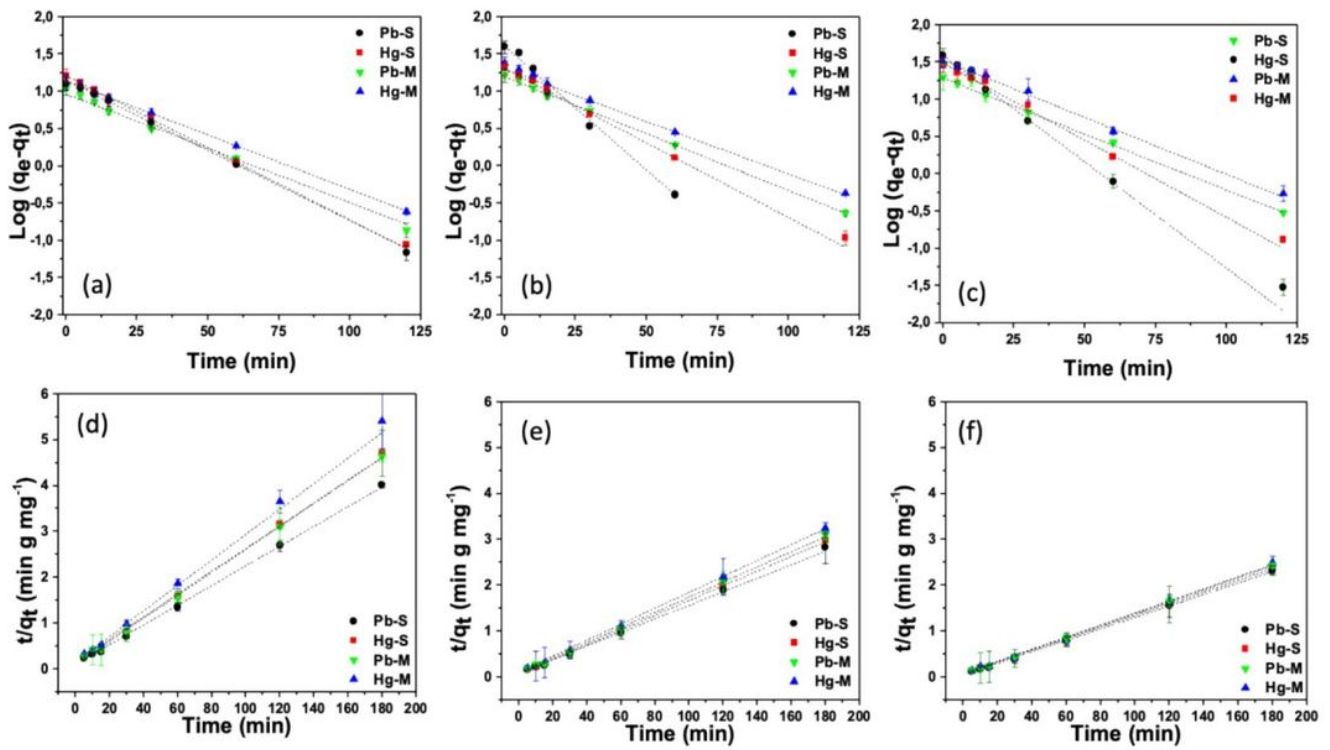


Figure 4

Kinetic models of pseudo first-order (PFO) for (a) Imo, (b) nZVI, and (c) Imo-nZVI and pseudo second-order (PSO) for (d) Imo, (e) nZVI, and (f) Imo-nZVI.

Fig. 5

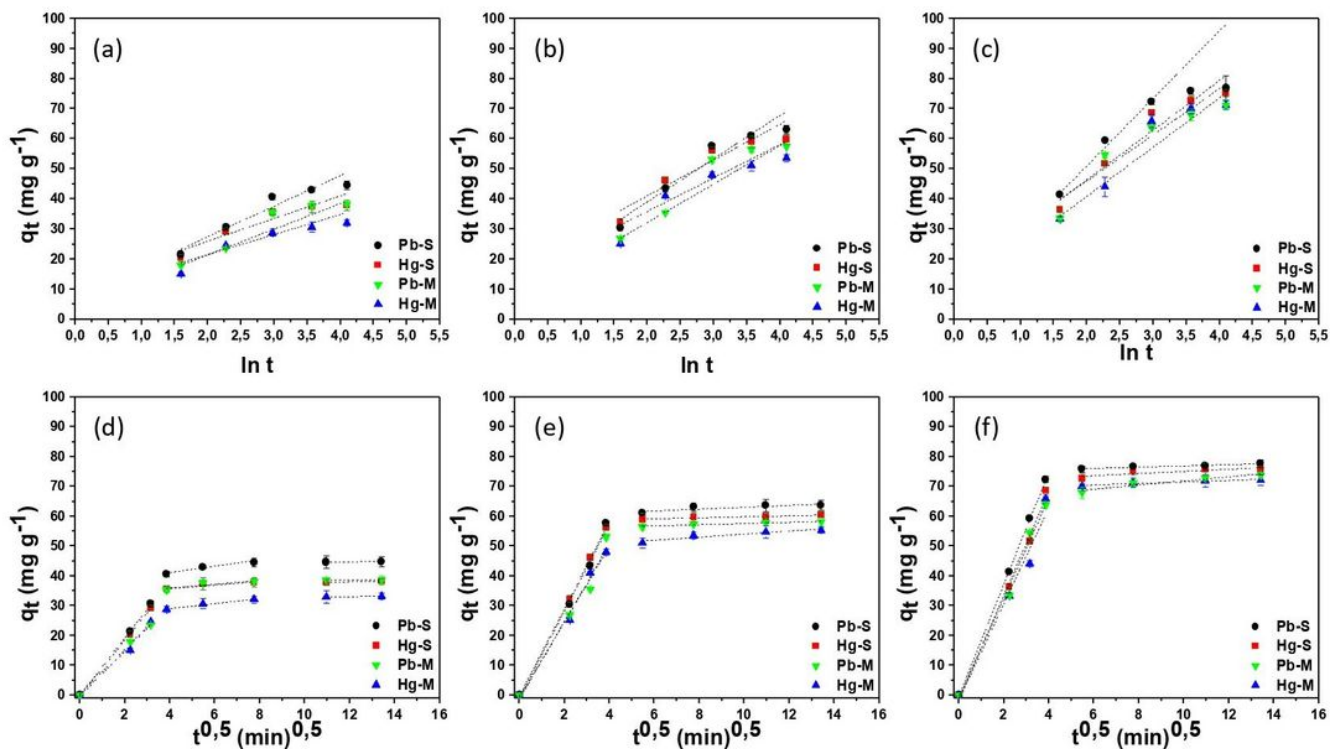


Figure 5

Fits of the experimental data to the Elovich equation for (a) imogolite, (b) nZVI, and (c) Imo-nZVI and Weber-Morris model for (d) Imo, (e) nZVI, and (f) Imo-nZVI.

Fig. 6

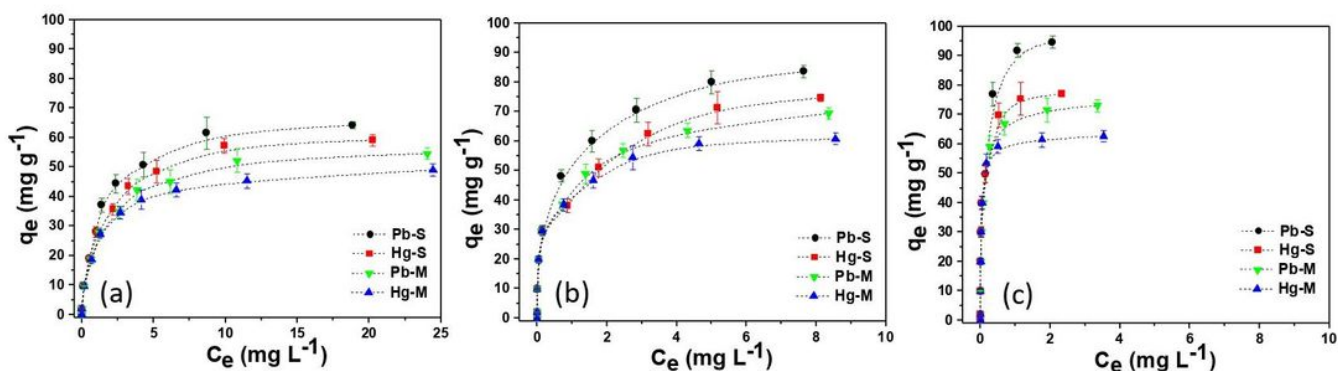


Figure 6

Langmuir isotherm for the adsorption of Pb^{2+} and Hg^{2+} in single (S) and multicomponent (M) systems on nZVI, Imo, and Imo-nZVI.

Fig. 7

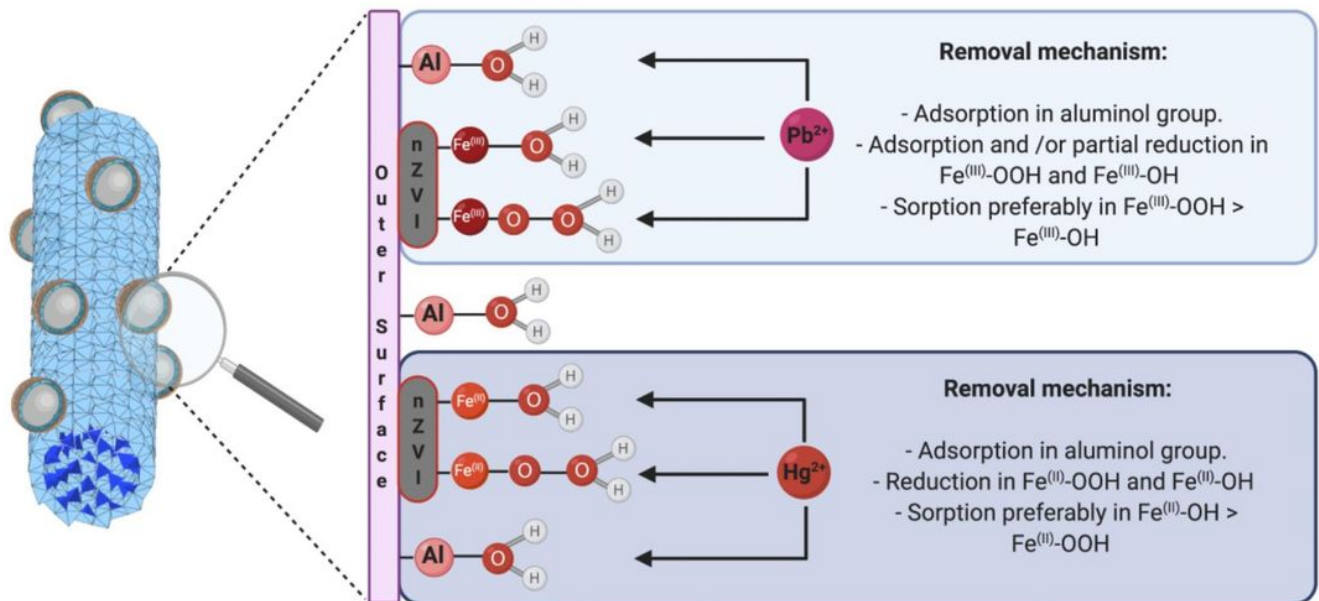


Figure 7

Schematic representation of the possible interactions that occur on the surface of the Imo-nZVI. The affinity and intensity of removal of Pb^{2+} and Hg^{2+} with the different groups of the nanocomposite is conditioned by the magnitude of the Misono softness parameters ($Y_{Hg^{2+}} = 4.24$ and $Y_{Pb^{2+}} = 3.58$) and the possibility they have of interacting with functional groups with similar characteristics.

Supplementary Files

This is a list of supplementary files associated with this preprint. Click to download.

- [S1.jpg](#)
- [S2.jpg](#)